

# The Lagrangian hydrodynamics code MAGMA2

S. Rosswog<sup>\*1</sup>

<sup>1</sup> *The Oskar Klein Centre, Department of Astronomy, AlbaNova, Stockholm University, SE-106 91 Stockholm, Sweden*

Draft version

## ABSTRACT

We present the methodology and performance of the new Lagrangian hydrodynamics code MAGMA2, a Smoothed Particle Hydrodynamics code that benefits from a number of non-standard enhancements. It uses high-order smoothing kernels and wherever gradients are needed, they are calculated via accurate matrix inversion techniques. Our default version does not make use of any kernel gradients, but a more conventional formulation has also been implemented for comparison purposes. MAGMA2 uses artificial viscosity, but enhanced by techniques that are commonly used in finite volume schemes such as reconstruction and slope limiting. While simple to implement, this approach efficiently suppresses particle noise, but at the same time drastically reduces dissipation in locations where it is not needed and actually unwanted. We demonstrate the performance of the new code in a number of challenging benchmark tests including e.g. complex, multi-dimensional Riemann problems and more astrophysical tests such as a collision between two stars to demonstrate its robustness and excellent conservation properties.

## 1 INTRODUCTION

A Lagrangian formulation of hydrodynamics is a natural choice for many astrophysical problems. Smoothed Particle Hydrodynamics (SPH) (Lucy 1977; Monaghan 1977) is the most wide-spread Lagrangian method in astrophysics. It is entirely mesh-free and the equations can be symmetrized in a way so that mass, energy, momentum and angular momentum are conserved by construction. As it is derived, SPH is entirely dissipationless and needs to be augmented by additional measures to produce appropriate amounts of entropy in shocks. This is traditionally done via artificial viscosity, but also Riemann solver approaches have been explored (Inutsuka 2002; Cha & Whitworth 2003; Cha et al. 2010; Murante et al. 2011; Puri & Ramachandran 2014).

In SPH one calculates the density via a smooth weighting of nearby particle masses and this smooth density estimate enters the calculation of pressures that drive the motion. The internal energy, in contrast, is evolved via a straight-forward discretization of the Lagrangian energy conservation law and does therefore not involve a smoothing process. This potentially different inherent smoothness of both quantities can lead to unintended “pressure blips” when setting up contact discontinuities. These blips cause surface tension effects that can suppress weakly triggered fluid instabilities (Agertz et al. 2007; McNally et al. 2012). Such effects can be counterbalanced by a careful setup of initial conditions with consistent smoothness, by alternative expressions for SPH volume elements (Ritchie & Thomas 2001; Saitoh & Makino 2013; Hopkins 2013; Rosswog 2015a; Cabezón et al. 2017) or by adding artificial conductivity terms to smooth out sharp transitions in the internal energy (Price 2008; Valdarnini 2012).

These issues have spurred further developments on Lagrangian hydrodynamics, many of which have employed techniques from finite volume Eulerian hydrodynamics. The `Arepo` code (Springel 2010a), for example, tessellates space into Voronoi cells and evolves the hydrodynamic equations via a Riemann solver-based finite vol-

ume strategy. Such finite volume approaches, however, are not bound to Voronoi or other meshes and can actually also be applied to hydrodynamic schemes which use particles. Several such finite volume particle schemes have been suggested in the applied mathematics literature (Ben Moussa et al. 1999; Vila 1999; Hietel et al. 2000; Junk 2003), but they have only recently found their way into astrophysics (Gaburov & Nitadori 2011; Hopkins 2015; Hubber et al. 2018) where they have delivered accurate results.

Also on the SPH-side there have been several new developments. Apart from the above mentioned volume element improvements, substantially more accurate estimates have been implemented (García-Senz et al. 2012; Cabezón et al. 2012; Rosswog 2015a). The perhaps most advanced SPH scheme to date (Frontiere et al. 2017) uses a reproducing kernel methodology (Liu et al. 1995) together with a sophisticated artificial dissipation scheme. They find good performance in a number of benchmark tests that are generally considered difficult for SPH. While the increasing cross-fertilization between different methods has led to higher accuracy, the boundaries between different them and the naming conventions have started to blur.

In this paper we describe the new Lagrangian hydrodynamics code MAGMA2, an SPH code that benefits from many improvements compared to more traditional SPH methods. It uses, for example, high-order kernels, calculates gradients via matrix-inversion techniques and uses slope-limited velocity reconstructions within an artificial viscosity approach. Many of these techniques have been scrutinized in a both Newtonian and special-relativistic context in Rosswog (2015a). The artificial viscosity approach that we are using is oriented at the recent work by Frontiere et al. (2017) which use fixed dissipation parameters, but reduce the effective viscosity by linearly reconstructing the velocities to inter-particle midpoints. We further expand on these ideas here and also keep the dissipation parameters fixed throughout this paper. A novel way to steer time-dependent dissipation parameters via entropy violations is ex-

arXiv:1911.13093v1 [astro-ph.IM] 29 Nov 2019

## 2 Rosswog

plored in a separate study (Rosswog 2019). The main purpose of this paper is to document MAGMA2 as a new simulation tool and to demonstrate its performance in a series of benchmark tests.

The paper is structured as follows. In Sec. 2 we describe the methodology used in MAGMA2 and Sec. 3 is dedicated to benchmark tests. We begin with smooth advection, then various shock tests, subsequently explore Kelvin-Helmholtz and Rayleigh-Taylor instabilities and combined, vorticity-creating shocks. We conclude our test series with astrophysical tests such as stellar collisions and tidal disruption events that demonstrate the versatility, robustness and the excellent conservation properties in practical examples. Sec. 4 briefly summarizes our study.

### 2 METHODOLOGY

The code MAGMA2 has been written from scratch in clean and modular Fortran95/2003. We have paid particular attention to separate technical infrastructure (such as the tree for neighbour search) from the physical modules. The choices for the hydrodynamics equations are mostly informed by our recent work (Rosswog 2015a) where we have carefully explored various SPH design choices such as the calculation of gradients, dissipation triggers or kernel functions. We only briefly summarize methods where this is possible and discuss the MAGMA2 choices more extensively where needed.

For a general introduction to the Smooth Particle Hydrodynamics (SPH) method, we refer to review articles (Monaghan 2005; Springel 2010b; Price 2012; Rosswog 2015b), a detailed step-by-step derivation of both Newtonian and relativistic SPH can be found in Rosswog (2009).

#### 2.1 Ideal hydrodynamics

We have implemented two SPH formulations in MAGMA2 both of which use high-order kernels and a novel dissipation scheme. The only difference between them is the way in which pressure-gradient terms are calculated. Our default choice uses accurate gradients that are calculated via a matrix inversion technique, see Sec. 2.1.1. We have also implemented a more conventional SPH formulation that is based on calculating gradients via kernel derivatives, see Sec. 2.1.2.

##### 2.1.1 Matrix inversion formulation

The standard SPH-approach of using direct gradients of (radial) kernel functions is a straight-forward way to ensure exact conservation<sup>1</sup>. The resulting gradients, however, are of moderate accuracy only (Abel 2011; Garcia-Senz et al. 2012; Cabezon et al. 2012; Rosswog 2015a,b; Cabezon et al. 2017). Improvements of many orders of magnitude in gradient accuracy can be achieved, see Fig. 1 in Rosswog (2015a) at the (low) price of inverting a 3x3-matrix (in 3D). We implement such a matrix-inversion SPH formulation

<sup>1</sup> See e.g. Sec.2.4 of Rosswog (2009) for detailed discussion of conservation in SPH. "Exact conservation" means up to potential violations due to finite accuracy due to time integration or approximations of the gravitational forces, e.g. due to the use of a tree. These latter terms, however, are usually fully controllable, though at some computational expense.

as default in MAGMA2 :

$$\rho_a = \sum_b m_b W_{ab}(h_a), \quad (1)$$

$$\frac{d\vec{v}_a}{dt} = -\sum_b m_b \left\{ \frac{P_a}{\rho_a^2} \vec{G}_a + \frac{P_b}{\rho_b^2} \vec{G}_b \right\}, \quad (2)$$

$$\left( \frac{du_a}{dt} \right) = \frac{P_a}{\rho_a^2} \sum_b m_b \vec{v}_{ab} \cdot \vec{G}_a, \quad (3)$$

where  $\rho, \vec{v}, u$  and  $h$  denote mass density, velocity, specific internal energy and smoothing length. The particle mass is denoted by  $m$ ,  $P$  is the gas pressure,  $\vec{v}_{ab} = \vec{v}_a - \vec{v}_b$  and  $W$  is the chosen SPH kernel function. This formulation is the Newtonian limit of a relativistic set of equations that was derived and extensively tested in Rosswog (2015a)<sup>2</sup>. The gradient functions are given by

$$\left( \vec{G}_a \right)^k = \sum_{d=1}^D C^{kd}(\vec{r}_a, h_a) (\vec{r}_b - \vec{r}_a)^d W_{ab}(h_a), \quad (4)$$

$$\left( \vec{G}_b \right)^k = \sum_{d=1}^D C^{kd}(\vec{r}_b, h_b) (\vec{r}_b - \vec{r}_a)^d W_{ab}(h_b), \quad (5)$$

where  $W_{ab}(h) = W(|\vec{r}_a - \vec{r}_b|, h)$  and the "correction matrix"  $C$  accounts for the local particle distribution and is calculated via matrix inversion

$$\left( C^{ki}(\vec{r}, h) \right) = \left( \sum_b \frac{m_b}{\rho_b} (\vec{r}_b - \vec{r})^k (\vec{r}_b - \vec{r})^i W(|\vec{r} - \vec{r}_b|, h) \right)^{-1}. \quad (6)$$

The functions  $\vec{G}_k$  are anti-symmetric with respect to the exchange of the involved position vectors and therefore allow for exact conservation in a similar way as the anti-symmetric  $\nabla_a W_{ab}$  in standard SPH. For more details we refer to Rosswog (2015a). The practical conservation will be scrutinized below in a violent, off-center collision between two stars, see Sec. 3.5.2, which shows that this formulation is on par with standard SPH in terms of numerical conservation.

##### 2.1.2 Standard kernel gradient formulation

For comparison we have also implemented a kernel-gradient formulation

$$\frac{d\vec{v}_a}{dt} = -\sum_b m_b \left\{ \frac{P_a}{\rho_a^2} \nabla_a W_{ab}(h_a) + \frac{P_b}{\rho_b^2} \nabla_a W_{ab}(h_b) \right\}, \quad (7)$$

$$\frac{du_a}{dt} = \frac{P_a}{\rho_a^2} \sum_b m_b \vec{v}_{ab} \cdot \nabla_a W_{ab}(h_a), \quad (8)$$

where the density is calculated as in our default version, see Eq. (1). This equation set can be derived from a Lagrangian (Monaghan & Price 2001; Springel & Hernquist 2002), but note that we have for simplicity omitted the so-called "grad-h terms" that contain derivatives of the kernel with respect to the smoothing length. These terms further improve the numerical conservation, but our tests in Rosswog & Price (2007) have shown that the violations of exact conservation are very small, even under conditions that are considered as "worst case" (Hernquist 1993). This will be further confirmed in our collision test in Sec. 3.5.2.

<sup>2</sup> The corresponding formulation was called  $\mathcal{F}_3$  in the original paper.

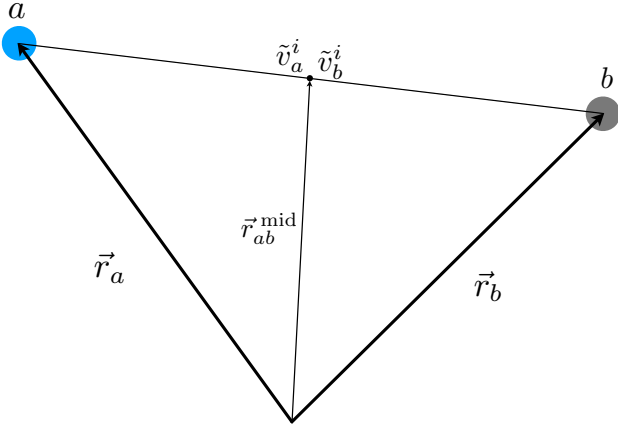


**Figure 1.** The artificial dissipation scheme uses the difference of the velocities reconstructed from particle  $a$  and particle  $b$  to their inter-particle midpoint at  $\vec{r}_{ab}$ .

## 2.2 Dissipation with reconstruction and slope-limiting

### 2.2.1 Artificial viscosity

A common approach to deal with shocks is to enhance the physical pressure  $P$  by additional viscous pressure terms  $Q$  (von Neumann & Richtmyer 1950), i.e. to replace the physical pressure, wherever it occurs, by  $P + Q$ . The pressures  $Q$  are typically the sum two terms, one is proportional to the velocity jump between computational elements (either cells or particles) while the other is proportional to the square of the jump. In SPH, the expression for the viscous pressure at particle position  $a$  is often written as (Monaghan & Gingold 1983)

$$Q_a = \rho_a \left( -\alpha c_{s,a} \mu_a + \beta \mu_a^2 \right), \quad (9)$$

where the velocity jump is

$$\mu_a = \min \left( 0, \frac{v_{ab}^\delta \eta_a^\delta}{\eta_a^2 + \epsilon^2} \right). \quad (10)$$

Here,  $\alpha$ ,  $\beta$  and  $\epsilon$  are numerical parameters (typical values are 1, 2 and 0.1),  $c_s$  is the sound speed and

$$\eta_a^\delta = \frac{(\vec{r}_a - \vec{r}_b)^\delta}{h_a}, \quad \eta_a^2 = \sum_\delta \eta_a^\delta \eta_a^\delta \quad (11)$$

are separations between particles, de-dimensionalized via the smoothing length  $h_a$ . We follow the convention that particles are labelled usually by  $a$  and  $b$  and we use greek letters to denote summation indices (such as the  $\delta$  above).

In SPH it is common practice to use  $v_{ab}^\delta = v_a^\delta - v_b^\delta$  in Eq. (10), i.e. to apply the velocity difference between the two particles. One can think of artificial dissipation as a simple way of solving an inter-particle Riemann problem (Monaghan 1997). Translated to the language of finite volume methods, the common practice of using straight forwardly the differences between particle velocities corresponds to a zeroth-order, or constant, velocity reconstruction. Zeroth-order reconstruction is known to introduce excessive dissipation in finite volume methods, but higher order reconstructions yield successively less dissipative numerical schemes. This idea is translated here into an SPH context. Most modern SPH implementations use time-dependent dissipation

parameters to avoid excessive and unnecessary dissipation (Morris & Monaghan 1997; Rosswog et al. 2000; Cullen & Dehnen 2010; Rosswog 2015a; Wadsley et al. 2017; Price et al. 2018). Recently, Frontiere et al. (2017), following ideas from a Eulerian finite volume context (Christensen 1990), have explored an alternative refinement where the same form of artificial pressure, Eq. (9), is used, but the velocity is (in their approach linearly) reconstructed to the particle midpoint. While still being a simple artificial viscosity scheme their scheme showed excellent performance even with fixed dissipation parameters  $\alpha$  and  $\beta$ . This motivates us to follow a similar approach.

Instead of using the difference of the two velocities, we quadratically reconstruct the velocities of particle  $a$  and  $b$  to their midpoint at  $\vec{r}_{ab}^{\text{mid}} = 0.5(\vec{r}_a + \vec{r}_b)$ , see Fig. 1. The velocities reconstructed from particle  $a$  read

$$\tilde{v}_a^i = v_a^i + \Phi_{ab} \left[ (\partial_j v^i) \delta^j + \frac{1}{2} (\partial_l \partial_m v^i) \delta^l \delta^m \right]_a, \quad (12)$$

where  $\Phi_{ab}$  is a slope limiter, see below, the index at the square bracket indicates that the derivatives at the position of particle  $a$  are used and the increments from point  $a$  to the midpoint are  $(\delta^i)_a = \frac{1}{2}(\vec{r}_b - \vec{r}_a)^i$ . The reconstructed velocities from the  $b$ -side,  $\tilde{v}_b^i$ , are calculated correspondingly, but now with derivatives at position  $b$  and increments  $\delta_b^i = -\delta_a^i$ . In Eq. (10) we use the difference in the *reconstructed* velocities, i.e.  $v_{ab}^\delta = \tilde{v}_a^\delta - \tilde{v}_b^\delta$ . We calculate the first derivatives as in Rosswog (2015a)

$$(\partial_j v^i)_a = C_a^{jk} \sum_b \frac{m_b}{\rho_b} [v_b^i - v_a^i] (\vec{r}_b - \vec{r}_a)^k W_{ab}(h_a), \quad (13)$$

where  $C$  is the correction matrix from Eq. (6). For the second derivatives we proceed in two steps. First, we calculate an auxiliary gradient that does not require the density (Price 2004; Rosswog & Price 2007) and therefore can be conveniently calculated alongside the density loop

$$(\partial_j v^i)_a^{\text{aux}} \equiv D_a^{jk} \sum_b m_b (v_b^i - v_a^i) \partial_k W_{ab}(h_a), \quad (14)$$

where the corresponding density-independent correction matrix is given by

$$D_a^{jk} = \left\{ \sum_b m_b (\vec{r}_b - \vec{r}_a)^j \partial_k W_{ab}(h_a) \right\}^{-1}. \quad (15)$$

The second derivatives are then calculated by applying Eq. (13) to the auxiliary first derivatives  $(\partial_j v^i)_a^{\text{aux}}$ . While this procedure to calculate second derivatives still comes at some cost, it does not require an additional loop over the neighbour particles compared to just linear reconstruction.

We use a modification of van Leer's slope limiter (van Leer 1974; Frontiere et al. 2017)

$$\Phi_{ab} = \max \left[ 0, \min \left[ 1, \frac{4A_{ab}}{(1 + A_{ab})^2} \right] \right] \begin{cases} 1, & \text{if } \eta_{ab} > \eta_{\text{crit}} \\ e^{-\left(\frac{\eta_{ab} - \eta_{\text{crit}}}{0.2}\right)^2}, & \text{otherwise} \end{cases} \quad (16)$$

with

$$A_{ab} = \frac{(\partial_\delta v_a^\gamma) x_{ab}^\delta x_{ab}^\gamma}{(\partial_\delta v_b^\gamma) x_{ab}^\delta x_{ab}^\gamma} \quad (17)$$

where the  $x_{ab}^\delta$  are the components of  $\vec{r}_a - \vec{r}_b$  and

$$\eta_{ab} = \min(\eta_a, \eta_b) = \min \left( \frac{r_{ab}}{h_a}, \frac{r_{ab}}{h_b} \right) \text{ and } \eta_{\text{crit}} = \left( \frac{32\pi}{3N_{\text{nei}}} \right)^{1/3}, \quad (18)$$

## 4 Rosswog

with  $r_{ab} = |\vec{r}_a - \vec{r}_b|$  and  $N_{\text{nei}}$  being the number of neighbours for the chosen kernel. This prescription yields excellent, oscillation-free shock results as we demonstrate below.

### 2.2.2 Artificial conductivity

The analogy with Riemann solvers (Monaghan 1997; Chow & Monaghan 1997; Price 2008) also suggests to include thermal conductivity in the artificial dissipation terms. Such approaches have been found advantageous in certain shock problems (Noh 1987; Rosswog & Price 2007), but –as with all artificial dissipation terms– one has to ensure that no unwanted side effects are introduced. We add an artificial conductivity term to our energy equation

$$\left(\frac{du_a}{dt}\right)_C = -\alpha_u \sum_b m_b \frac{v_{\text{sig},u}^{ab}}{\rho_{ab}} (\tilde{u}_a - \tilde{u}_b) \frac{|\vec{G}_a + \vec{G}_b|}{2}, \quad (19)$$

where for the standard gradient version the average of the  $\vec{G}$ -terms is replaced by  $[\nabla_a W_{ab}(h_a) + \nabla_a W_{ab}(h_b)]/2$ . As for the velocities in the artificial viscosity, we use the differences in the quadratically reconstructed internal energies at the interparticle midpoint,  $\tilde{u}_a$  and  $\tilde{u}_b$ , which are calculated analogously to the velocities. For the conductivity signal velocity we use

$$v_{\text{sig},u}^{ab} = (1 - iG)v_{\text{sig},nG}^{ab} + iGv_{\text{sig},G}^{ab}, \quad (20)$$

where  $iG$  is a flag indicating whether gravity is used ( $iG = 1$ ) or not ( $iG = 0$ ) and

$$v_{\text{sig},nG}^{ab} = \sqrt{\frac{|P_a - P_b|}{\rho_{ab}}} \quad \text{and} \quad v_{\text{sig},G}^{ab} = |\vec{v}_a - \vec{v}_b|. \quad (21)$$

These expressions are very similar to those used in the PHANTOM code (Price et al. 2018), but, as with the artificial viscosity terms, we are using here differences in the reconstructed velocities and internal energies (as indicated by tildes) rather than “flat” differences and matrix-inversion based gradient functions.

Throughout this study, we always use constant dissipation parameters  $\alpha = 1$  and  $\beta = 2\alpha$ . As we will demonstrate below, and consistent with a similar approach in a reproducing kernel context (Frontiere et al. 2017), the described velocity reconstruction produces excellent results and reduces drastically unwanted effects of artificial viscosity. Nevertheless, one may still try to additionally steer the dissipation parameter  $\alpha$  so that –if it safe to do so– it decays towards zero. A novel way of steering  $\alpha$  will be explored in a separate study (Rosswog 2019).

For the conductivity parameter we use a conservatively low value of  $\alpha_u = 0.05$  as default choice. While we found conductivity beneficial in instabilities, we have not encountered any negative side effect, see for example, the test in Sec. 3.5.1. Price et al. (2018) use a value of unity and report that they have not encountered artifacts for even this large value.

## 2.3 Kernel choice

SPH needs a kernel function to estimate densities and gradients, see Eqs.(1) - (8). Cubic spline kernels (Schoenberg 1946; Monaghan 2005) have traditionally been the standard choice in SPH. In recent years, however, a number of alternatives have been explored, see, for example, Cabezón et al. (2008); Read et al. (2010); Dehnen & Aly (2012); Rosswog (2015a). In particular the family of Wendland kernels (Wendland 1995) has received a fair amount of attention, because they avoid the so-called “pairing instability” (Schüssler

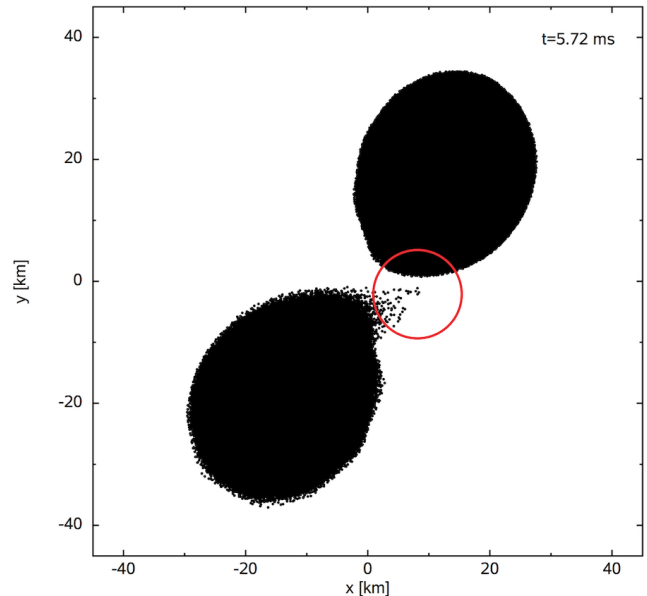


**Figure 2.** Astrophysical example (merger of a 1.3 with a 1.4  $M_{\odot}$  neutron star) where an expanding flow encounters a sharp surface with a very large SPH particle density. The smoothing length of the leading particle is indicated by the red circle.

& Schmitt 1981) as pointed out by Dehnen & Aly (2012). While these kernels require a large neighbour number for an accurate density and gradient estimate, see Figs. 4 and 5 in Rosswog (2015a), they are exceptionally good at keeping an ordered particle distribution<sup>3</sup> and in suppressing sub-resolution noise. We had experimented with other high-order kernels (Rosswog 2015a) and in static density and gradient estimation tests on fixed particle lattices they actually showed better accuracy than the Wendland kernels. In dynamic tests, however, the Wendland kernels delivered more ordered particle distributions and were overall the better choice. To illustrate this, compare the high-order  $W_{h,9}$  and the  $C^6$  Wendland kernel (WC6)<sup>4</sup> in Figs. 4 and 11 in Rosswog (2015a).

Here we use the WC6 kernel as a default and choose the smoothing length so that there are exactly 300 neighbours within the  $2h_a$ -support of each particle  $a$ , see Sec. 2.5,  $h_a$  being the particle’s smoothing length. We have performed a few tests where we changed to a different kernel function, however, we hardly noticed any difference. We show in the context of Rayleigh-Taylor instabilities below an example where we compare our default choice with a kernel from the sinc-kernel family (Cabezón et al. 2008). Some small differences are visible that are consistent with the sinc kernel producing slightly more noisy results and therefore seeding more Rayleigh-Taylor plumes.

## 2.4 Neighbour search and gravitational forces

We use a “recursive coordinate bisection” (RCB) tree (Gafton & Rosswog 2011) to search for neighbour particles and to calculate gravitational forces. The main idea is to start from a cuboid that contains all the particles and then recursively split the longest side

<sup>3</sup> For an illustration see, e.g., Fig. 2 in Rosswog (2015b).

<sup>4</sup> In Rosswog (2015a) we referred to this kernel as  $W_{3,3}$ .

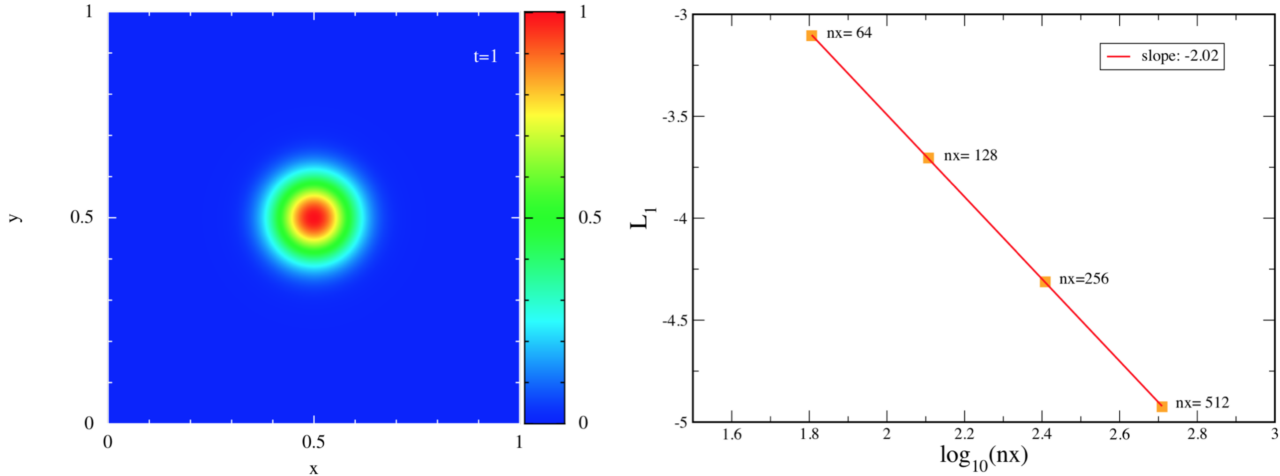


**Figure 3.** Advection of a smooth Gaussian pulse. Left: density distribution, right:  $L_1$ -error as function of number of points in x-direction  $n_x$ .

of each cuboid so that it contains (to high accuracy) the same number of particles in each resulting daughter cell. The procedure is repeated until, on the deepest level of the tree, each cell contains no more than  $N_{ll}$  particles. Such cells are referred to as lowest-level or ll-cells. We use  $N_{ll} = 12$ , but as shown in our original paper (Gafton & Rosswog 2011), the results are not very sensitive to this choice. Our tree yields very simple integer relations between different nodes in the tree, so that nodes can be addressed via simple integer arithmetics. The tree is not walked down for each particle, but instead only for each ll-cell. This means that the number of required tree-walks to find the neighbour particles is reduced by a factor of  $\approx N_{ll}$ . As a result of a neighbour tree walk, the tree returns a list of potential neighbour particles (“candidates”). Also for gravity, we only descend the tree for the centre of mass of each ll-cell, the forces at the particle positions within the ll-cell are obtained via a high-order Taylor-expansion. As shown in our original paper, this tree-build is for  $4 \times 10^6$  particles approximately 30 faster than the Press tree (Benz et al. 1990). Neighbour search and gravity are at this particle number about a factor of 6 faster with our RCB with the discrepancy becoming increasingly larger for higher particle numbers  $N$ . Our RCB-tree scales close to  $O(N)$  while the Press tree scales like most tree methods proportional to  $O(N \log N)$ . Similar to the hydrodynamic equations, one can also derive the gravitational accelerations consistently from a Lagrangian (Price & Monaghan 2007) and the resulting equations contain corrective, “gravitational grad-h terms”. Consistent with our treatment of hydrodynamics, we also neglect the grad-h terms here, so that the gravitational acceleration reads

$$\left(\frac{d\vec{v}_a}{dt}\right)_{\text{grav}} = -G \sum_b m_b \left[ \frac{\Phi'_{ab}(h_a) + \Phi'_{ab}(h_b)}{2} \right] \hat{e}_{ab}, \quad (22)$$

where  $\hat{e}_{ab} = (\vec{r}_a - \vec{r}_b)/|\vec{r}_a - \vec{r}_b|$  and the gravitational potential that is used for monitoring the total energy

$$\Phi_a = G \sum_b m_b \Phi_{ab}(h_a). \quad (23)$$

The gravitational smoothing kernel for the force,  $\Phi'$ , and for the gravitational potential,  $\Phi$ , can be calculated directly from the density kernel  $W$  via

$$\Phi'(r, h) = \frac{4\pi}{r^2} \int_0^r W(r', h) r'^2 dr' \quad (24)$$

$$\Phi(r, h) = 4\pi \left[ -\frac{1}{r} \int_0^r W(r', h) r'^2 dr' + \int_0^r W(r', h) r' dr' - \int_0^{Qh} W(r', h) r' dr' \right]. \quad (25)$$

For commonly used density kernels  $W$  these integrals can be solved analytically. However, to make it possible to change  $W$  with minimal changes in the code, we calculate  $\Phi'$  and  $\Phi$  numerically and tabulate all kernels, so that for a different choice of  $W$  automatically the consistent kernels  $\Phi'$  and  $\Phi$  are available for force and potential calculation.

As stressed in our original paper, large speed gains can be obtained when variables are mapped into a “tree-vector” in exactly the order in which they are addressed during the tree-walk. We have followed this strategy in all computationally expensive parts of the tree, e.g. the direct gravitational force calculation from nearby particles, but also generally throughout MAGMA2.

## 2.5 Adaption of smoothing lengths

The so-called “grad-h terms” (Springel & Hernquist 2002; Monaghan 2002) have originally been introduced to ensure exact conservation. For pragmatic reasons, however, we set them to unity since consistent update of smoothing length and density requires an iteration between the two which comes at a non-negligible computational expense. More importantly for us, our earlier experiments (Rosswog & Price 2007) showed that while the conservation properties improved somewhat, these were rather small corrections to an already excellent conservation. Even in a violent head-on collision of two stars, historically considered a “worst case scenario” for energy conservation in SPH (Hernquist 1993), the relative energy conservation was better than  $\approx 10^{-3}$ , even when ignoring the grad-h terms. These results are consistent with those presented below, see Sec. 3.5.2. Finally, and most relevant for our decision to *not* use an iteration between  $\rho$  and  $h$ , is that we kept running into numerical problems when an expanding flow suddenly encounters a sharp surface with a very large number density of SPH particles. Such an example, the merger of two neutron stars with 1.3 and 1.4  $M_\odot$  is shown in Fig 2: the density of the first particles that flow over the inner Lagrange point towards the heavier neutron star drops rapidly, thereby causing a strong increase in the smoothing lengths. Once close enough, the particles suddenly encounter the

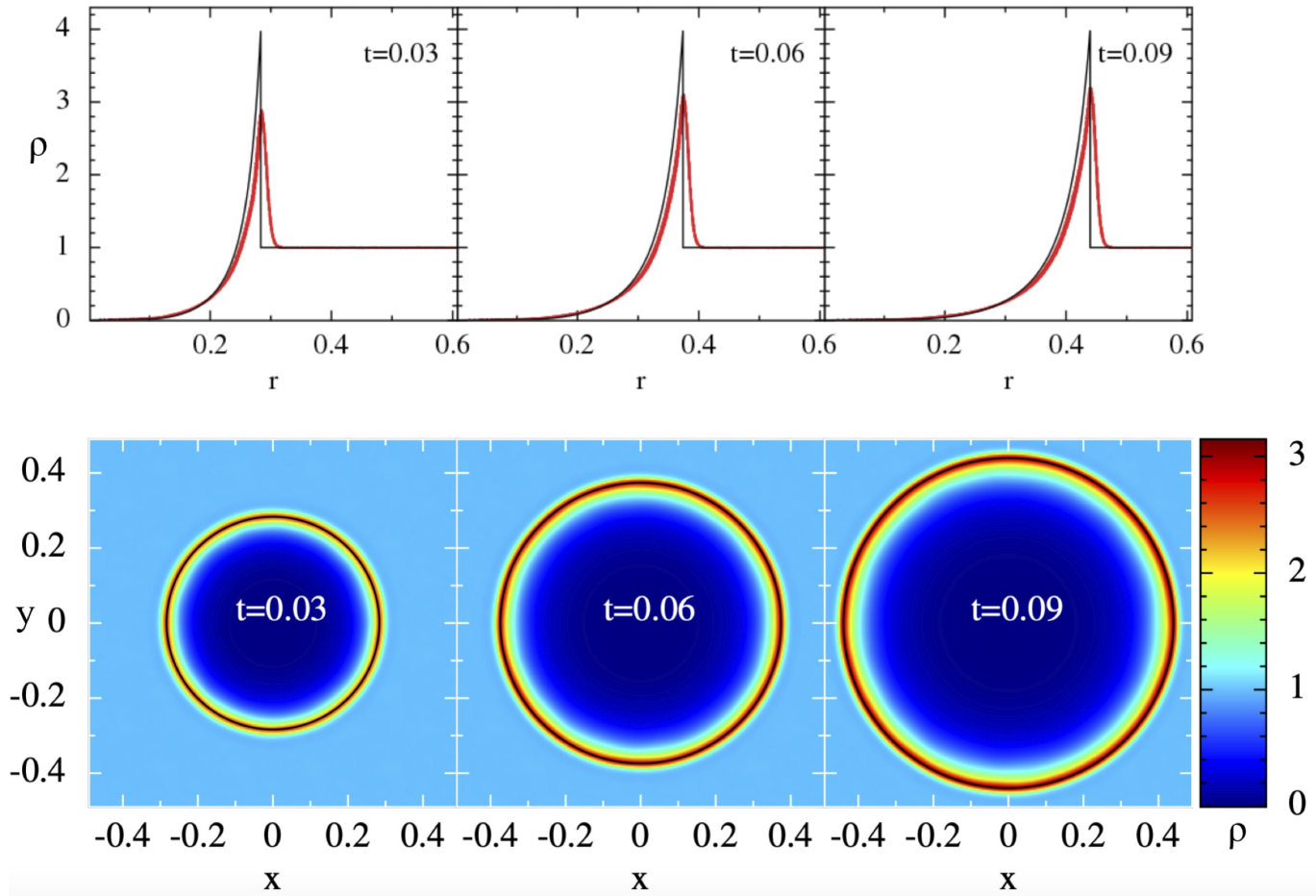


**Figure 4.** Time evolution of a Sedov blast ( $128^3$  particles), all particles are plotted in the upper row panels. Note the absence of any visible deviations from spherical symmetry.

other neutron star with an enormous particle number density. It is a challenge to assign a good value for the smoothing length  $h$  of such front particles since a tiny change in  $h$  can easily change the neighbour number by an order of magnitude. This can lead to problems with the size of neighbour lists or –in case counter measures are taken– this can lead to very erratic changes of the smoothing length of this particle and therefore to a substantial amount of numerical noise.

To avoid such problems, we *assign to each particle an exact neighbour number before its force is calculated*. We first build our RCB-tree with smoothing lengths that are 10% larger than those from the previous time step. A neighbour tree walk then returns a substantially longer candidate list for each “lowest-level cell” than the desired neighbour number  $n_{\text{des}}$  of each particle. From this candidate list the particle with the  $(n_{\text{des}} + 1)$ th largest distance to the particle of interest  $a$  is selected via a partitioning algorithm (Press et al. 1992) and this distance sets the interaction length  $h_a$ .

Although this algorithm may seem at first sight very computationally expensive, it is actually not: if we calculate all the derivatives needed for an SPH simulation for the case of a star made of  $5 \times 10^6$  particles, the assignment of the smoothing length takes only  $\approx 7\%$  of the total time to calculate the derivatives (usually dominated by self-gravity). Apart from being very robust in extreme situations, this procedure has the additional advantage that the smooth-

ing lengths evolve very smoothly and without introducing unnecessary noise.

## 2.6 Time integration

We perform all shown tests with the total variation diminishing (TVD) second order Runge-Kutta (RK2) method (Gottlieb & Shu 1998)

$$y^* = y^n + \Delta t f(y^n) \quad (26)$$

$$y^{n+1} = \frac{1}{2} [y^n + y^* + \Delta t f(y^*)]. \quad (27)$$

If desired, the derivatives  $f(y^*)$  can be “recycled” for the next prediction step, so that only one derivative is effectively calculated per time step. We have implemented this option as a simple switch, so that we can choose whether one or two derivatives are calculated per time step. We have explored the accuracy of this “force-recycling” in practical tests, but have not found noticeable differences in any of them. Nevertheless, we use the TVD RK2 integrator with two derivative calculations in our tests.

The time step is chosen as minimum from a “force-” and “Courant-criterion” (Monaghan 1992)

$$\Delta t = C \min(\Delta t_f, \Delta t_C) \quad (28)$$

where

$$\Delta t_f = \min_a \left( \sqrt{\frac{h_a}{|\vec{f}_a|}} \right), \quad (29)$$

$$\Delta t_C = \min_a \left( \frac{h_a}{c_a + 0.6\alpha(c_a + 2\max_b(\mu_{ab}))} \right). \quad (30)$$

and for the prefactor we choose  $C = 0.2$ . While being very simple and efficient, this time integration algorithm provides excellent numerical conservation of energy and angular momentum, as we will show below.

### 3 TESTS

We begin with an advection test to measure the order of convergence in smooth flows. We then show a number of shocks and a Kelvin-Helmholtz and a Rayleigh-Taylor instability test. We further show combined tests where shocks go along with vorticity creation and we conclude with astrophysical tests, a stellar collision and a tidal disruption, that demonstrate MAGMA2's robustness for practical applications.

As pointed out earlier (Rosswog 2015a) the initial conditions are crucial for the accuracy of an SPH simulation, but unfortunately it is sometimes non-trivial to construct initial conditions with all the desired properties. The particles should be distributed with high regularity so that they guarantee a high interpolation accuracy (see, e.g., Sec. 3 of Rosswog (2015a) for an accurate interpolation quality indicators). This is, however, not enough, since the particle distribution should also not contain any preferred directions, but simple lattices usually do. This may lead to artefacts such as the piling up of particles in a shock along the grid direction, see Fig. 17 in Rosswog (2015a) for an illustration.

All of the tests shown below are performed with the full 3D code. "2D" tests are performed by simulating a slice that is thick enough for the central plane not to be affected by edge effects. We often simply proceed with particles set up on a cubic lattice (CL). While this is not a perfect setup since the particles are not in stable equilibrium configuration, we get away with it in many cases. Slightly more complex is the setup in a "close-packed" (CP) lattice which we apply in some tests. While the CP setup is preferred over the CL (Rosswog 2015a), it still contains preferred directions which can cause artefacts, e.g. in the Sedov explosion test. For such cases we resort to (patches of) *Centroidal Voronoi Tessellations* (CVT) (Du et al. 1999) for which we have not found any artefact.

#### 3.1 Smooth advection

In this test we place a Gaussian density pulse of initial shape

$$\rho^i(x, y) = (\rho_2 - \rho_1) \exp \left[ -\frac{(x-0.5)^2 + (y-0.5)^2}{\sigma^2} \right] + \rho_1, \quad (31)$$

where  $\rho_1 = 10^{-3}$ ,  $\rho_2 = 1$  and  $\sigma = 0.1$  in a (quasi)-2D box with  $[0, 1] \times [0, 1]$ , see Fig. 3, left panel. The gas with polytropic index  $\Gamma = 5/3$  is represented by 20 CL-layers of  $n_x \times n_x$  particles in X- and Y-direction. The density profile is advected with uniform pressure  $P_0 = 10^{-6}$  and velocity  $v_x = 1$  through the box with periodic boundaries. After crossing the box once the  $L_1$ -error,  $L_1 = \sum_b^N |\rho^i(\vec{r}_b) - \rho_b|/N$ , is measured. The  $L_1$ -results for different resolutions  $n_x$  are plotted in the right panel of Fig. 3. The measured slope is  $-2.02$ , very close to the 2nd order that is theoretically expected for our code.

### 3.2 Shocks

#### 3.2.1 3D Sedov-Taylor explosion

The Sedov-Taylor explosion test, a strong, initially point-like blast into a low density environment, has an analytic self-similarity solution (Sedov 1959; Taylor 1950). For an explosion energy  $E$  and a density of the ambient medium  $\rho$ , the blast wave propagates after a time  $t$  to the radius  $r(t) = \beta(Et^2/\rho)^{1/5}$ , where  $\beta$  depends on the adiabatic exponent of the gas ( $\approx 1.15$  in 3D for the  $\Gamma = 5/3$  that we are using). Directly at the shock front, the density jumps by the strong-explosion limit factor of  $\rho_2/\rho_1 = (\Gamma + 1)/(\Gamma - 1) = 4$ , where we have inserted  $\Gamma = 5/3$ . Behind the shock the density drops quickly and finally vanishes at the centre of the explosion.

To set up the test numerically, we distribute a given number of SPH particles according to the CVT prescription in the computational volume  $[-0.5, 0.5] \times [-0.5, 0.5] \times [-0.5, 0.5]$  and assign them masses so that their density is  $\rho = 1$ . This is done in an iterative way where we first assign a guess value for the masses, then measure the resulting density via Eq. (1) and subsequently correct the particle masses. The iteration is stopped once the density agrees everywhere to better than 0.5% with the desired value. The energy  $E = 1$  is spread across a very small initial radius  $R$  and it is entirely distributed as internal energy, the specific internal energy  $u$  of the particles outside of  $R$  is entirely negligible ( $10^{-10}$  of the central  $u$ ). For the initial radius  $R$  we choose twice the interaction radius of the innermost SPH particle. Boundaries play no role in this test as long as the blast does not interact with them. We therefore place "frozen" particles around the computational volume as boundary particles. Fig. 4 shows the result for  $128^3$  particles (red, every particle is plotted) together with the exact solution (black line). The overall agreement is very good and there are no noticeable deviations from spherical symmetry. Note in particular the absence of density oscillations in the wake of the shock. Such oscillations plague even modern SPH-simulations of this test, see for example Rosswog & Price (2007); Hu et al. (2014); Cabezon et al. (2017); Wadsley et al. (2017); Frontiere et al. (2017). The peak height could easily be raised by using a lower order kernel with fewer neighbours, if one was willing to accept more post-shock noise (which we are not). We also show, see Fig. 5, Sedov tests with increasing resolution of  $64^3$ ,  $128^3$  and  $256^3$  SPH particles within  $[-0.5, 0.5]^3$ .

#### 3.2.2 3D Sod shock

The "Sod shock tube" (Sod 1978) is a classic code test to ensure the correctness of a hydrodynamics code implementation. As initial conditions we use

$$(\rho, \vec{v}, P) = \begin{cases} (1.000, 0, 0, 0, 1.0) & \text{for } x < 0. \\ (0.125, 0, 0, 0, 0.1) & \text{else.} \end{cases} \quad (32)$$

and  $\Gamma = 5/3$ . In most SPH papers this test is only shown in 1D. Here we perform a quasi-1D test with the 3D code, employing  $400 \times 24 \times 24$  particles placed in  $[-0.5, 0.5] \times [-0.03, 0.03] \times [-0.03, 0.03]$ . The use of the WC6 kernel with its large neighbour number together with the new dissipation prescription makes our implementation substantially more robust against artefacts from details of the initial particle setup. Here even the simplest approach with particles placed on a uniform cubic lattice gives good results, see Fig. 6. The numerical results (all particles are shown) agree well with the exact solution, there is only a small velocity overshoot at the shock front and small over-/undershoots at one of the edges of the rarefaction region ( $x \approx -0.05$ ).

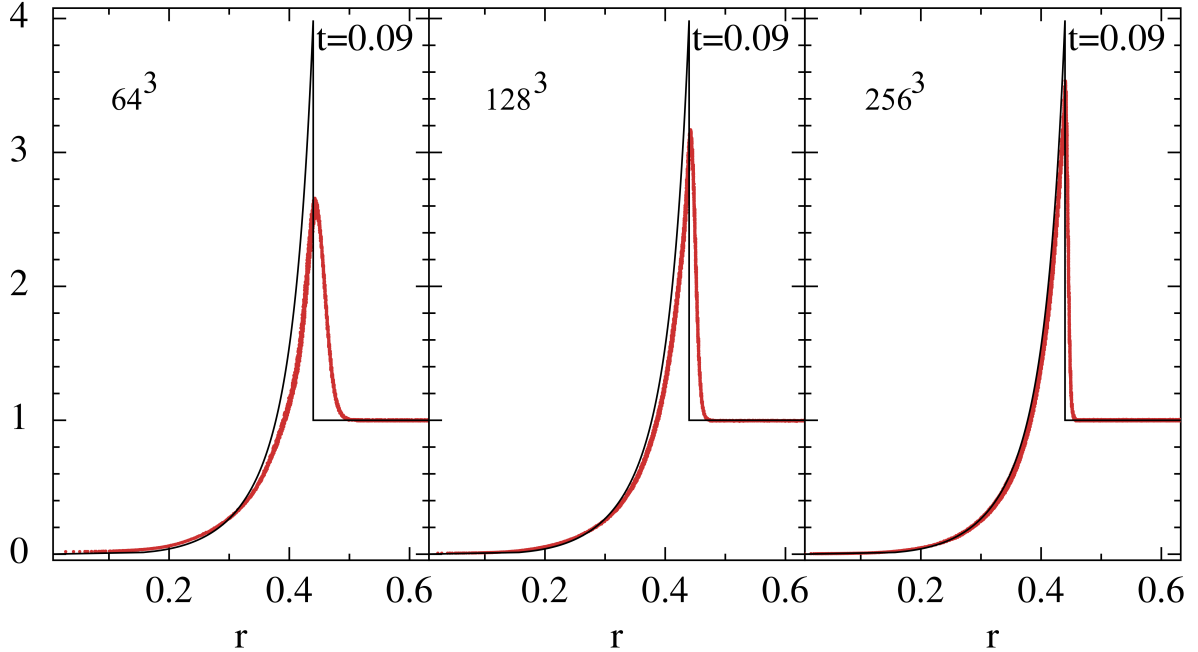


**Figure 5.** Sedov blast of increasing resolution ( $64^3$ ,  $128^3$ ,  $256^3$  particles), all particles are plotted.

### 3.2.3 3D strong blast wave

A substantially more challenging version of the Sod test, the so-called strong blast wave test, is set up with initial conditions

$$(\rho, \vec{v}, P) = \begin{cases} (1.0, 0, 0, 0, 1000.0) & \text{for } x < 0 \\ (1.0, 0, 0, 0, 0.1) & \text{else} \end{cases} \quad (33)$$

and with  $\Gamma = 1.4$ . Again we set up this test as quasi-1D with our 3D code in an analogous way to the Sod test with  $800 \times 24 \times 24$  particles between  $[-0.5, 0.5]$  in x-direction. The result at time  $t = 0.01$  is shown in Fig. 7. Overall, the numerical result is in very good agreement with the exact solution, but there are small overshoot in density and dips in pressure and velocity at the contact discontinuity.

### 3.2.4 Spherical blast wave 1

As another benchmark we use a three-dimensional shock-tube problem. We follow Toro (1999) in the parameter choice (apart from a shift of the origin): the computational domain is  $[-1, 1]^3$  and the initial conditions are chosen as:

$$(\rho, \vec{v}, P) = \begin{cases} (1.000, 0, 0, 0, 1.0) & \text{for } r < 0.5 \\ (0.125, 0, 0, 0, 0.1) & \text{else.} \end{cases} \quad (34)$$

The solution exhibits a spherical shock wave, a spherical contact surface traveling in the same direction and a spherical rarefaction wave traveling towards the origin. We show the MAGMA2 solution ( $200^3$  particles, cubic lattice) at time  $t = 0.2$  in Fig. 8. We show in the upper row the density,  $|v|$  and pressure at  $t = 0.2$  in the XY-plane. In the lower row, we compare the SPH-result ( $|y| < 0.018, |z| < 0.018$ ) with a reference solution obtained by the Eulerian weighted average flux method with  $400^3$  grid cells (Toro

1999). The SPH solution is essentially oscillation-free and in very close agreement with the reference solution. Only the sharp edges (e.g. in  $|v|$  near  $|x| \approx 0.3$ ) are somewhat smoothed out and there is a small oscillation in the pressure at the contact discontinuity.

### 3.2.5 Spherical blast wave 2

As a second spherical blast wave problem (Toro 1999) we start from

$$(\rho, \vec{v}, P) = \begin{cases} (1.0, 0, 0, 0, 2.0) & \text{for } r < 0.5 \\ (1.0, 0, 0, 0, 1.0) & \text{else.} \end{cases} \quad (35)$$

We show the numerical solution ( $200^3$  particles, cubic lattice) at time  $t = 0.2$  in Fig. 9. Again, the SPH result is in very good agreement with the (higher resolved) reference solution, only the inner density plateau is somewhat smeared out, and there is a small wiggle at the contact discontinuity. This could be cured, for example, by applying a larger amount of conductivity (keep in mind we only use a small value,  $\alpha_a = 0.05$ ). Note that in both circular blast wave problems the spherical symmetry is very well preserved, despite the initial particle setup on a cubic lattice.

### 3.2.6 Noh test

Next we consider the very challenging 3D Noh implosion test (Noh 1987) which has the reputation as "code breaker", since a number of established methods are not able to handle this test without breaking or simply producing wrong results (Liska & Wendroff 2003). The test is performed with a polytropic exponent of  $\Gamma = 5/3$  and with initial conditions  $[\rho_0, v_0^i, P_0] = [1, -\hat{r}_a^i, 10^{-10}]$ ,

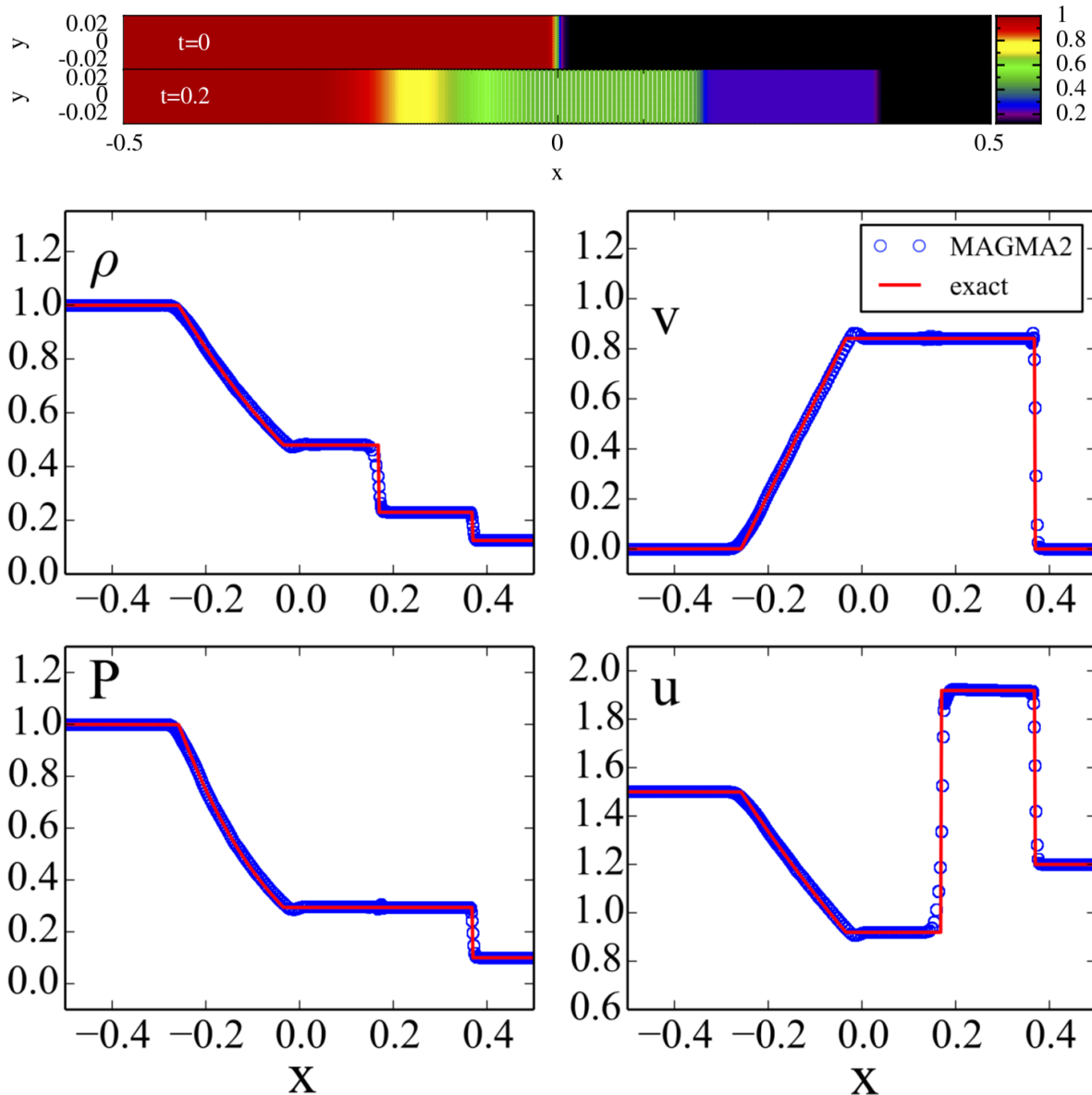


**Figure 6.** Sod shock test performed in 3D with  $400 \times 24 \times 24$  particles. The upper two panels show the particle distribution (density is colour-coded) at  $t=0$  and  $t=0.2$ . The four panels below show (upper left to lower right) density, velocity, pressure and internal energy of all particles at  $t=0.2$  together with the exact solution (red). All particles are plotted.

where  $\hat{r}_a^i$  is the  $i$ -component of the radial unit vector of particle  $a$ . This corresponds to the spherical inflow to a point and results in a self-similar shock moving outwards at a velocity  $v_s = 1/3$ . The shocked region ( $r < v_s t$ ) has density  $\rho_s = \rho_0 [(\Gamma + 1)/(\Gamma - 1)]^3$ . The pre-shock flow ( $r > v_s t$ ) undergoes shock-less compression according to  $\rho(r, t) = \rho_0 (1 - v_0 t/r)^2$ .

The test is challenging for two reasons. First, the initial conditions contain an unresolved point of convergence that gives rise to the well-known “wall heating problem” where the thermal energy overshoots at the origin while the density undershoots in order to strive for the correct pressure. This phenomenon lead to the original suggestion to apply an artificial conductivity (Noh 1987) to alleviate the problem. The second difficulty is that the adiabatic pre-shock compression should not produce entropy which is a serious challenge for most artificial viscosity schemes.

We have setup this challenging test with both a CL and a CVT configuration. Both show small artefacts of comparable size. We show in Fig. 10 the density for this test (for the CL setup) for our default parameter choice,  $\rho$ ,  $v$  and  $P$  are shown in Fig. 11 compared with the exact solution<sup>5</sup>. Despite the CL setup the inner shocked region is perfectly spherically symmetric. At the centre the “wall-heating problem” with a substantial density undershoot is encountered and the pressure is about 4% below the theoretical value. Nevertheless, compared to most existing methods MAGMA2 performs reasonably well in this challenging test. The wall heating effect could be alleviated by employing larger  $\alpha_{ul}$ -values. The PHANTOM code (Price et al. 2018), for example, uses  $\alpha_{ul} = 1$  and the authors report to have not found serious artefacts from this large value. However,

<sup>5</sup> <http://cococubed.asu.edu>

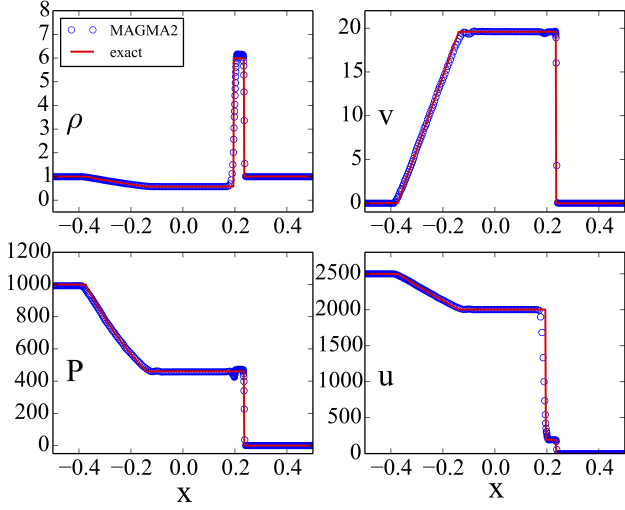


**Figure 7.** 3D strong blast wave test at  $t = 0.01$  ( $800 \times 24 \times 24$  particles).

given the somewhat pathological initial conditions with its unresolved point of convergence, we are not excessively worried about the encountered wall-heating problem (that is shared by most other methods) and do not see this as a strong incentive to increase the dissipation parameter  $\alpha_{ul}$  beyond the chosen, low value.

### 3.3 Instabilities

#### 3.3.1 Kelvin-Helmholtz Instability

Kelvin-Helmholtz (KH) instabilities occur in shear flows with a perturbed interface. They play an important role in astrophysics and occur in a broad range of environments, e.g. in mixing processes in novae (Casanova et al. 2011), amplification of magnetic fields in neutron star mergers (Price & Rosswog 2006; Giacomazzo et al. 2014; Kiuchi et al. 2015) or planetary atmospheres (Johnson et al. 2014), to name just a few. Traditional versions of SPH, however, have been shown to struggle with weakly triggered KH-instabilities (Agertz et al. 2007; McNally et al. 2012). We focus here on a test setup in which traditional SPH has been shown to fail, even at rather high resolution in 2D, see McNally et al. (2012). We follow the latter paper in setting up the test with the only difference that we use our full 3D code to perform the test in quasi-2D. To this end we set up a thin 3D slice with  $N \times N \times 20$  particles (referred to as “ $N^2$ ”), for simplicity initially placed on a cubic lattice. Periodic boundary conditions are obtained by placing appropriate particle copies outside of the “core” volume. The test is initialized as:

$$\rho(y) = \begin{cases} \rho_1 - \rho_m e^{(y-0.25)/\Delta} & \text{for } 0.00 \leq y < 0.25 \\ \rho_2 + \rho_m e^{(0.25-y)/\Delta} & \text{for } 0.25 \leq y < 0.50 \\ \rho_2 + \rho_m e^{(y-0.75)/\Delta} & \text{for } 0.50 \leq y < 0.75 \\ \rho_1 - \rho_m e^{(0.75-y)/\Delta} & \text{for } 0.75 \leq y < 1.00 \end{cases} \quad (36)$$

where  $\rho_1 = 1$ ,  $\rho_2 = 2$ ,  $\rho_m = (\rho_1 - \rho_2)/2$  and  $\Delta = 0.025$ . The velocity is set up as

$$v_x(y) = \begin{cases} v_1 - v_m e^{(y-0.25)/\Delta} & \text{for } 0.00 \leq y < 0.25 \\ v_2 + v_m e^{(0.25-y)/\Delta} & \text{for } 0.25 \leq y < 0.50 \\ v_2 + v_m e^{(y-0.75)/\Delta} & \text{for } 0.50 \leq y < 0.75 \\ v_1 - v_m e^{(0.75-y)/\Delta} & \text{for } 0.75 \leq y < 1.00 \end{cases} \quad (37)$$

with  $v_1 = 0.5$ ,  $v_2 = -0.5$ ,  $v_m = (v_1 - v_2)/2$  and a small velocity perturbation in  $y$ -direction is introduced as  $v_y = 0.01 \sin(2\pi x/\lambda)$

with the perturbation wave length  $\lambda = 0.5$ . In the linear regime, the instability grows on a time scale of

$$\tau_{KH} = \frac{(\rho_1 + \rho_2)\lambda}{\sqrt{\rho_1 \rho_2} |v_1 - v_2|}, \quad (38)$$

with  $\tau_{KH} \approx 1.06$  for the chosen parameters. The test is performed with a polytropic equation of state with exponent  $\Gamma = 5/3$ .

We show in Fig. 12 the evolution of the instability at times  $t = 1.5, 2.0$  and  $2.5$  for resolutions of  $128^2$ ,  $256^2$  and  $512^2$  particles and for our default choices. All cases grow at very similar rates and produce the characteristic “Kelvin-Helmholtz billows”, even at the lowest resolution. For comparison, traditional SPH implementations struggle with this only weakly triggered instability ( $v_y = 0.01$ ), see, for example, Fig. 9 of McNally et al. (2012), where even at a resolution  $512^2$  particles the instability hardly grows (for the cubic spline kernel, label “Ne512”) or much too slowly (for the quintic spline kernel, label “No512”). In Fig. 13 we show the mode growth (calculated exactly as in McNally et al. (2012)) for all our cases compared to a high-resolution reference solution ( $4096^2$  cells) obtained by the PENCIL code (Brandenburg & Dobler 2002). Even our low-resolution case with  $128^2$  particles is very close to the reference solution, the growth rates of the higher resolution cases are hard to distinguish from the reference solution.

It is instructive to repeat this test (at fixed resolution of  $256^2$  particles) and each time vary one of the choices we have made. Density snapshots of these experiments are shown in Fig. 14, the corresponding growth rates are shown in Fig. 15. As first line in Fig. 14 we show the results obtained with our default choices. For the results in line two we used the same choices, but only linear reconstruction; line three used no reconstruction at all; line four applied the default choices, but used kernel gradients (instead of matrix-inversion gradients) and, finally, line five used the cubic spline kernel with 50 neighbours rather than the WC6 kernel with 300 neighbours. The reconstruction has the largest impact in this test, which substantially reduces the net dissipation. The differences between the quadratic and linear reconstruction are only moderate, the interfaces between the high and low density parts remain sharper in the former case (this is confirmed by running the simulations for longer). Not using any reconstruction at all, i.e. applying the common SPH approach of using the velocity differences at the particle positions, suppresses the growth of the instability all together, see the magenta diamonds in Fig. 15. Note, however, that this could also be cured by applying time-dependent dissipation schemes (Morris & Monaghan 1997; Rosswog et al. 2000; Cullen & Dehnen 2010; Rosswog 2015a; Price et al. 2018). The version with standard gradients also shows healthy growth, albeit at a somewhat lower rate and at  $t = 1.5$  the edges of the high-density region are rather noisy. Although the cubic spline kernel has been found to be inferior to higher order kernels (Rosswog 2015a; Tricco 2019) it delivers in this test (together with matrix-gradients and large dissipation, but velocity reconstruction) satisfactory results.

#### 3.3.2 Rayleigh-Taylor instability

The Rayleigh-Taylor instability is a standard probe of the subsonic growth of a small perturbation. In its simplest form, a layer of density  $\rho_t$  rests on top of a layer with density  $\rho_b < \rho_t$  in a constant acceleration field, e.g. due to gravity. While the denser fluid sinks down, it develops a characteristic, “mushroom-like” pattern. Simulations with traditional SPH implementations have shown only retarded growth or even a complete suppression of the instability (Abel 2011; Saitoh & Makino 2013).

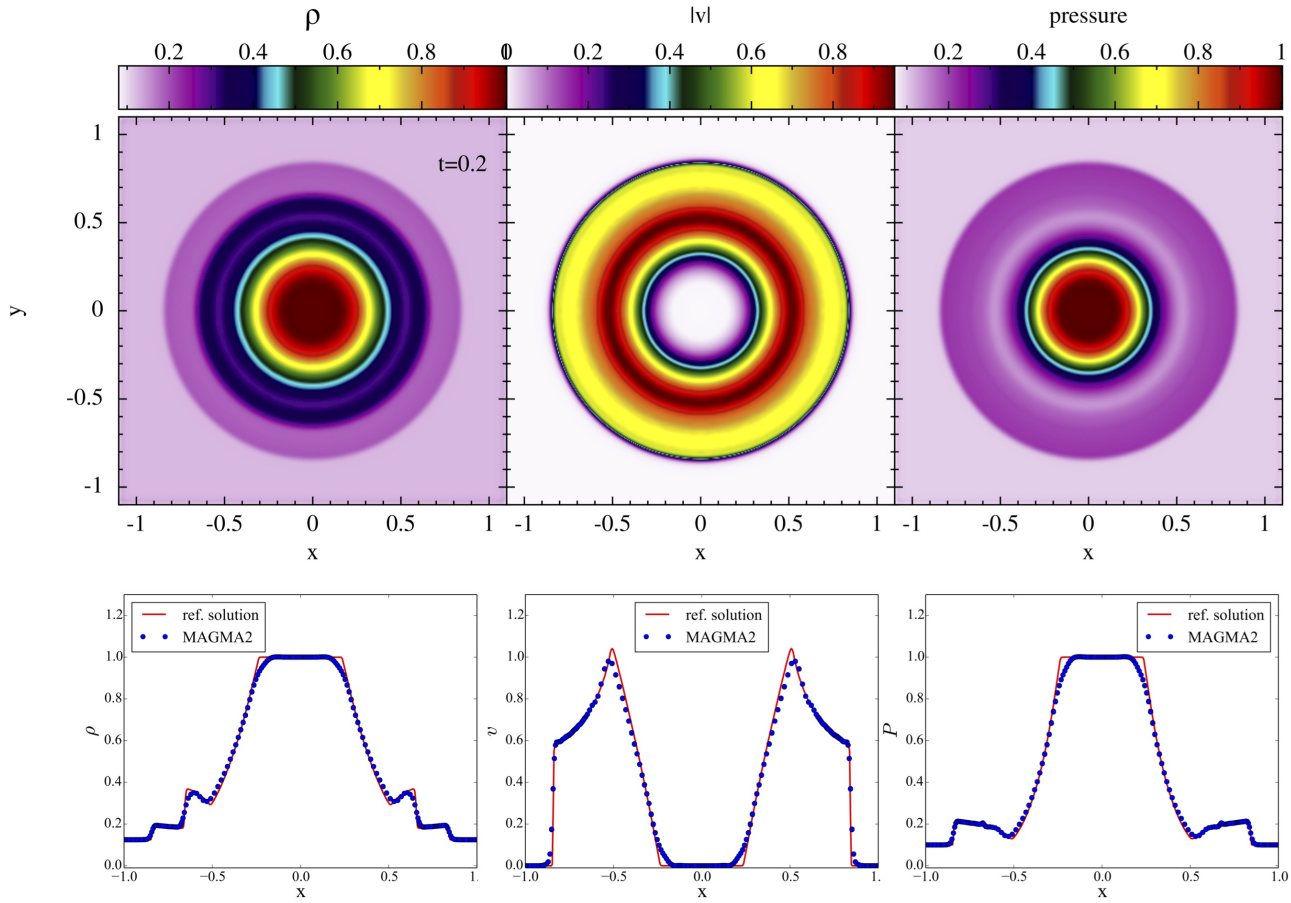


**Figure 8.** Circular blast wave problem 1 in 3D at  $t = 0.2$  ( $200^3$  particles). Upper row: MAGMA2 result for density,  $|v|$  and pressure. Lower row: corresponding quantities from MAGMA2 results compared with a reference solution (red line) obtained by the Eulerian weighted average flux method ( $400^3$  grid cells) (Toro 1999).

As before, we adopt a quasi-2D setup and use the full 3D code for the evolution. We place the particles on a CL in the XY-domain  $[-0.25, 0.25] \times [0, 1]$  and we use 8 layers of particles in the Z-direction. Similar to Frontiere et al. (2017) we use  $\rho_t = 2$ ,  $\rho_b = 1$ , a constant acceleration  $\vec{g} = -0.5\hat{e}_y$  and

$$\rho(y) = \rho_b + \frac{\rho_t - \rho_b}{1 + \exp[-(y - y_t)/\Delta]} \quad (39)$$

with transition width  $\Delta = 0.025$  and transition coordinate  $y_t = 0.5$ . We apply a small velocity perturbation to the interface

$$v_y(x, y) = \delta v_{y,0} [1 + \cos(8\pi x)] [1 + \cos(5\pi(y - y_t))] \quad (40)$$

for  $y$  in  $[0.3, 0.7]$  with an initial amplitude  $\delta v_{y,0} = 0.025$ , and use a polytropic equation of state with exponent  $\Gamma = 1.4$ . The equilibrium pressure profile is given by

$$P(y) = P_0 - g\rho(y)[y - y_t] \quad (41)$$

with  $P_0 = \rho_t/\Gamma$ , so that the sound speed is near unity in the transition region. To enforce boundary conditions we add 10 rows of extra particles ( $y > 1$  and  $y < 0$ ) that we “freeze” at the initial conditions and we use periodic boundary conditions elsewhere.

We show in Fig. 16 the results of several simulations at a time of  $t = 4$ . The first panel shows the result for a simulation that uses the standard SPH approach with kernel gradients and a XY-resolution of  $128 \times 256$  particles which overall performs reasonable

well. The second panel shows the results for everything else being the same, but using matrix-inversion kernels instead. This version delivers finer resolved/less diffusive density structures and a larger plunge depth. With increasing resolution the density transitions become sharper and more substructure appears, but the plunge depth remains the same.

This test is one of the very few where we see a small impact of the kernel choice. Our main motivation for using the  $C^6$  Wendland kernel as a default was that it leads to a particularly low level of particle noise (Rosswog 2015a). We have also experimented with the 7th order sinc-kernel WH7 (Cabezón et al. 2008) where we also use 300 neighbours. The results at time  $t = 3.7$  are shown in Fig. 17. Overall the agreement and in particular the plunge depth are very similar. But the WH7 result shows larger deviations from symmetry and a somewhat richer plume structure. This is consistent with being seeded by a larger amount of small scale noise for the WH7 kernel.

### 3.4 Complex shocks with vorticity creation

A set of challenging 2D benchmark tests has been suggested by Schulz-Rinne (1993). They are constructed in such a way that four constant states meet at one corner and the initial values are chosen so that one elementary wave, either a shock, a rarefaction or a

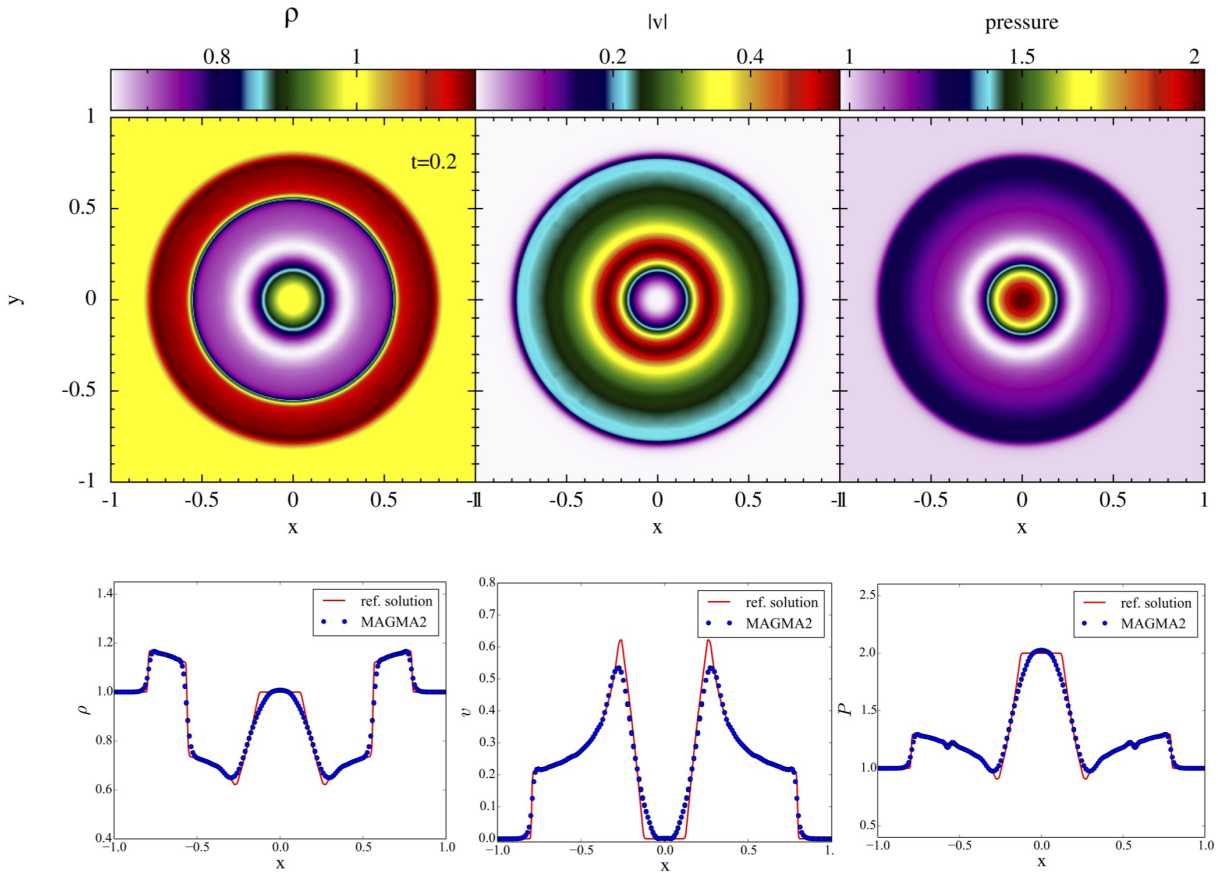


**Figure 9.** Circular blast wave problem 2 in 3D at  $t = 0.2$  ( $200^3$  particles). Upper row: MAGMA2 result for density,  $|v|$  and pressure. Lower row: corresponding quantities from MAGMA2 results compared with a reference solution (red line) obtained by the Eulerian weighted average flux method ( $400^3$  grid cells) (Toro 1999).

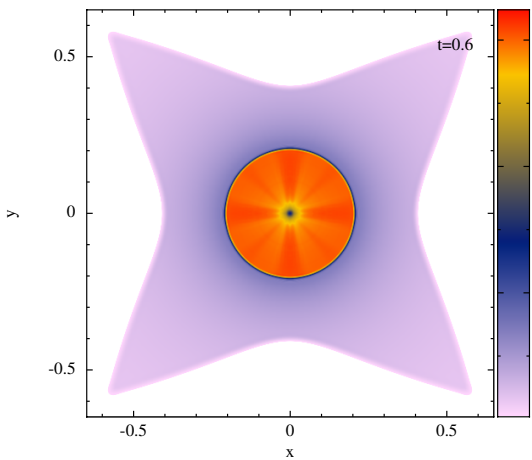


**Figure 10.** Result of the challenging 3D Noh implosion test with our default parameter set.. Shown is the density distribution in the XY-plane at  $t = 0.6$ .

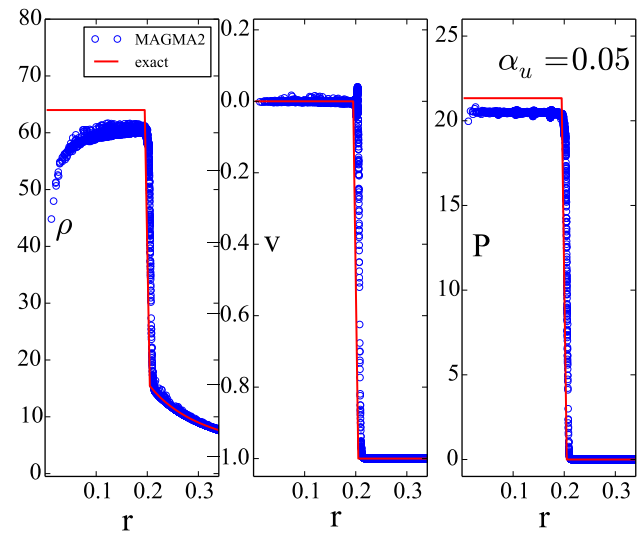


**Figure 11.** Result of the challenging 3D Noh implosion test, the exact solution is shown as solid red line.

contact discontinuity appears at each interface. During the subsequent evolution complex wave patterns emerge for which no exact solutions are known. These tests are considered challenging benchmarks for multi-dimensional hydrodynamics codes (Schulz-Rinne

1993; Lax & Liu 1998; Kurganov & Tadmor 2002; Liska & Wendroff 2003). Such tests are rarely shown for SPH codes, in fact, we are only aware of the work by Puri & Ramachandran (2014) who show results for one such shock test in a study of Godunov SPH

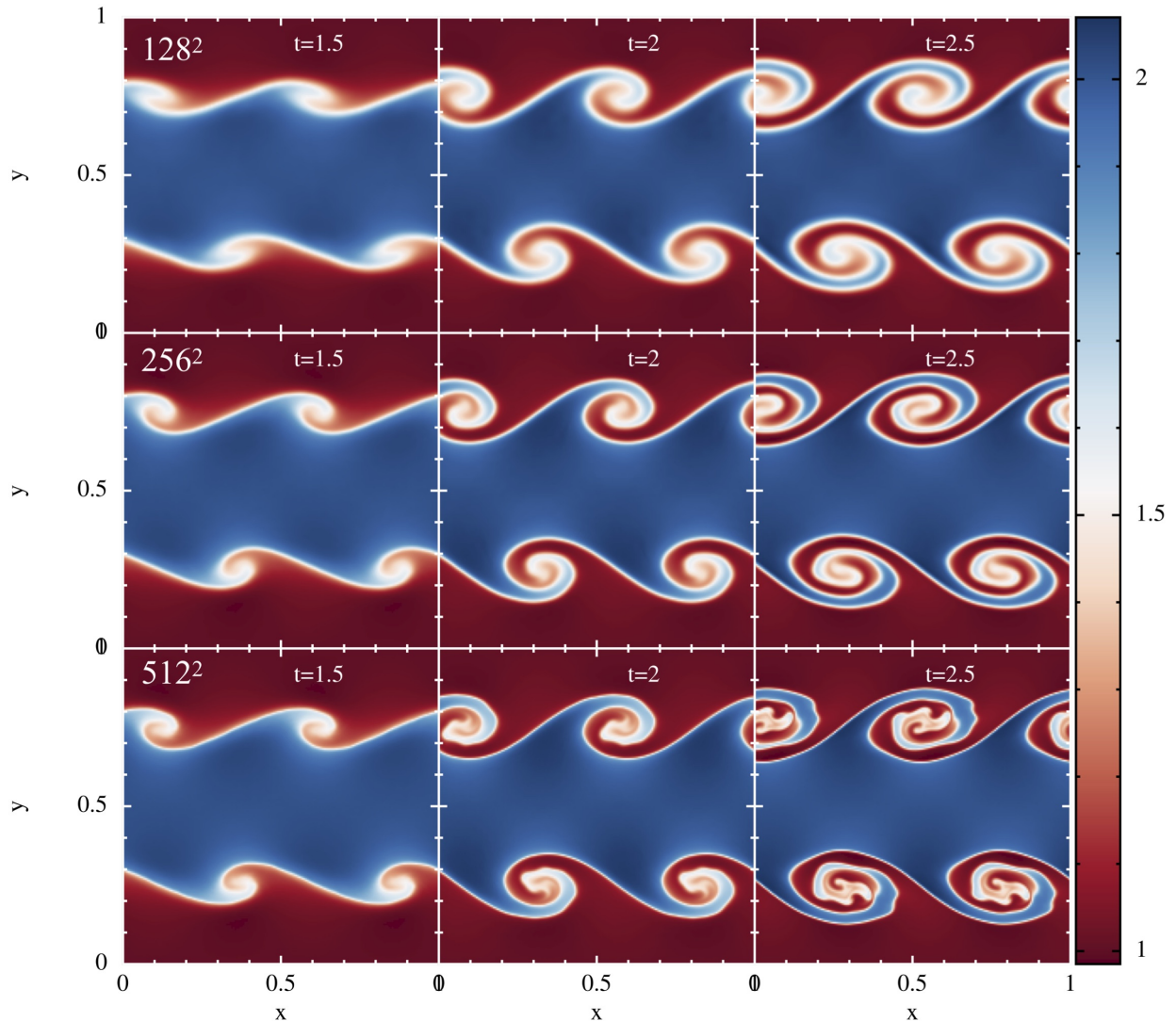


**Figure 12.** Density evolution for weakly triggered Kelvin-Helmholtz instability at  $(128 \times 128 \times 8)$ ,  $(256 \times 256 \times 8)$  and  $(512 \times 512 \times 8)$  particles resolution.

with approximate Riemann solvers.

Here we investigate six such configurations. Since our code is intrinsically 3D, we simulate, as before, a slice thick enough so that the midplane is unaffected by edge effects (we use 10 particle layers in Z-direction). We use  $660 \times 660$  particles in the XY-plane arranged on a hexagonal lattice between  $[x_c - 0.5, x_c + 0.5] \times [y_c - 0.5, y_c + 0.5]$ ,  $(x_c, y_c)$  being the contact point of the quadrants, and we use a polytropic exponent  $\Gamma = 1.4$  in all of the tests. We refer to these Schulz-Rinne type problems as SR1 - SR6 and give their initial parameters for each quadrant in Tab. 1. These test problems correspond to configuration 3, 4, 5, 6, 11 and 12 in the labelling convention of Kurganov & Tadmor (2002). Our results are shown in Fig. 18.

Test SR1 is the only one of the Schulz-Rinne tests that has to our knowledge been tackled with (Godunov-)SPH (Puri & Ramachandran 2014). Their results show that existing SPH implementations struggle to resolve the mushroom-like structure along the diagonal (roughly at  $x \approx y \approx 0.2$  in our figure, upper left panel) and depending on the chosen approximate Riemann solver serious artefacts appear. Our results, in contrast, show crisp transitions between the

different regions, well developed "mushrooms" and they look overall similar to those found with established Eulerian methods, see e.g. Liska & Wendroff (2003), their Fig.4.1. In test SR2 straight 1D shocks separating constant states and two curved shocks bordering a lens-shaped high-density/-pressure region occur. The result should be symmetric with respect to the lens axis and the MAGMA2 results do not show any noticeable deviation from perfect symmetry. Test SR3 yields a lense-shaped central region with two vortex structures occurring at the upper left and lower right part of the shown domain. Again, our result at  $t = 0.23$  closely resembles those in the literature, e.g. Lax & Liu (1998), their Fig.5. This is also true for the remaining tests, SR 4 can be compared, e.g. with Fig. 4.1 in Liska & Wendroff (2003), SR 5 with Fig. 11 in Lax & Liu (1998) and SR6 with Fig. 4.4 in Liska & Wendroff (2003). Note that all tests show a high (though not perfect) degree of symmetry which –with freely moving particles– is not actively enforced. Overall, the tests are in very good agreement with the Eulerian results found in the literature (Lax & Liu 1998; Liska & Wendroff 2003) and they look crisp and noise free. Note in particular the appearance of mushroom-like structures (in panels 1, 5 and 6) which

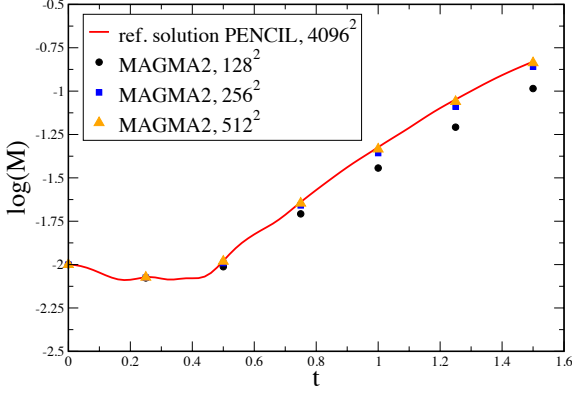


**Figure 13.** Growth of the Kelvin-Helmholtz mode amplitude for our default formulation as a function of resolution. As reference solution (solid, red) we use a simulation with the Pencil Code at a resolution of  $4096^2$ . Note that all cases show a growth close to the reference solution, even at the lowest resolution ( $128^2$  particles). For comparison, traditional SPH simulations struggle with this only weakly triggered test, even at substantially higher resolution of  $512^2$  (McNally et al. 2012).

are usually considered a challenge for SPH-methods. Some of the weak straight lines in the panels, however, are considered spurious. But these artefacts are shared by the majority of methods found in the literature.

### 3.5 Astrophysical applications

In this last section we show tests that are close to astrophysical applications. The purpose of these tests is to demonstrate the performance of the dissipation scheme, measure the numerical conservation in a relevant example and to show robustness and geometric flexibility.

#### 3.5.1 Oscillating White Dwarf

As another experiment, we take a relaxed  $\Gamma = 5/3$ -polytropic star that represents a model for a  $0.3 M_{\odot}$  WD. We use only 10K SPH particles and provide them with a radial velocity  $\vec{v}_a = v_0 \vec{r}_a$ , where we choose  $v_0 = 0.02$ . As before, all tests use constant dissipation parameters of  $\alpha = 1$ . To avoid dissipation from other sources, we run these tests with low tolerance for the tree accuracy ( $\Theta = 0.1$ ) and a time integration prefactor  $C = 0.1$ . The evolution of the oscillations in the gravitational energy are shown Fig. 19. As blue line we show the standard SPH-approach, i.e. without velocity reconstruction, the red line shows our default choice of methods and parameters and the black, open circles show the result for the default choices, but with  $\alpha_{it} = 0$ . Consistent with the experiments in the Kelvin-Helmholtz instability test, see Fig. 14, we find a massive suppression of unwanted dissipation when velocity reconstruction is employed. As intended, artificial conductivity does not switch on in this test problem, the results with  $\alpha_{it} = 0$  lie nearly exactly on top of the  $\alpha_{it} = 0.05$  (default).

**Table 1.** Initial data for the Schulz-Rinne-type 2D Riemann problems

SR1; contact point: (0.3, 0.3)				
variable	NW	NE	SW	SE
$\rho$	0.5323	1.5000	0.1380	0.5323
$v_x$	1.2060	0.0000	1.2060	0.0000
$v_y$	0.0000	0.0000	1.2060	1.2060
$P$	0.3000	1.5000	0.0290	0.3000
SR2; contact point: (-0.15, -0.15)				
variable	NW	NE	SW	SE
$\rho$	0.5065	1.1000	1.1000	0.5065
$v_x$	0.8939	0.0000	0.8939	0.0000
$v_y$	0.0000	0.0000	0.8939	0.8939
$P$	0.3500	1.1000	1.1000	0.3500
SR3; contact point: (0.0, 0.0)				
variable	NW	NE	SW	SE
$\rho$	2.0000	1.0000	1.0000	3.0000
$v_x$	-0.7500	-0.7500	0.7500	0.7500
$v_y$	0.5000	-0.5000	0.5000	-0.5000
$P$	1.0000	1.0000	1.0000	1.0000
SR4; contact point: (0.0, 0.0)				
variable	NW	NE	SW	SE
$\rho$	2.0000	1.0000	1.0000	3.0000
$v_x$	0.7500	0.7500	-0.7500	-0.7500
$v_y$	0.5000	-0.5000	0.5000	-0.5000
$P$	1.0000	1.0000	1.0000	1.0000
SR5; contact point: (0.0, 0.0)				
variable	NW	NE	SW	SE
$\rho$	0.5313	1.0000	0.8000	0.5313
$v_x$	0.8276	0.1000	0.1000	0.1000
$v_y$	0.0000	0.0000	0.0000	0.7276
$P$	0.4000	1.0000	0.4000	0.4000
SR6; contact point: (0.0, 0.0)				
variable	NW	NE	SW	SE
$\rho$	1.0000	0.5313	0.8000	1.0000
$v_x$	0.7276	0.0000	0.0000	0.0000
$v_y$	0.0000	0.0000	0.0000	0.7262
$P$	1.0000	0.4000	1.0000	1.0000

#### 3.5.2 Collision between two main sequence stars

Here we simulate a collision between two main sequence stars. The aim is, on the one hand, to demonstrate the robustness and usefulness for the simulation of violent astrophysical events and, on the other hand, to measure how accurately our new formulation numerically conserves physically conserved quantities for typical simulation parameters (tree opening criterion and time integration). For the simulation we choose two identical stars, each with a mass  $M_* = 1M_{\odot}$  and a radius  $R_* = R_{\odot}$ , modelled as a  $\Gamma = 5/3$  polytrope with  $2 \times 10^6$  equal mass SPH particles. The stars approach each other on a parabolic orbit with an impact strength

$$\beta \equiv \frac{2R_*}{R_{\text{peri}}} = 3. \quad (42)$$

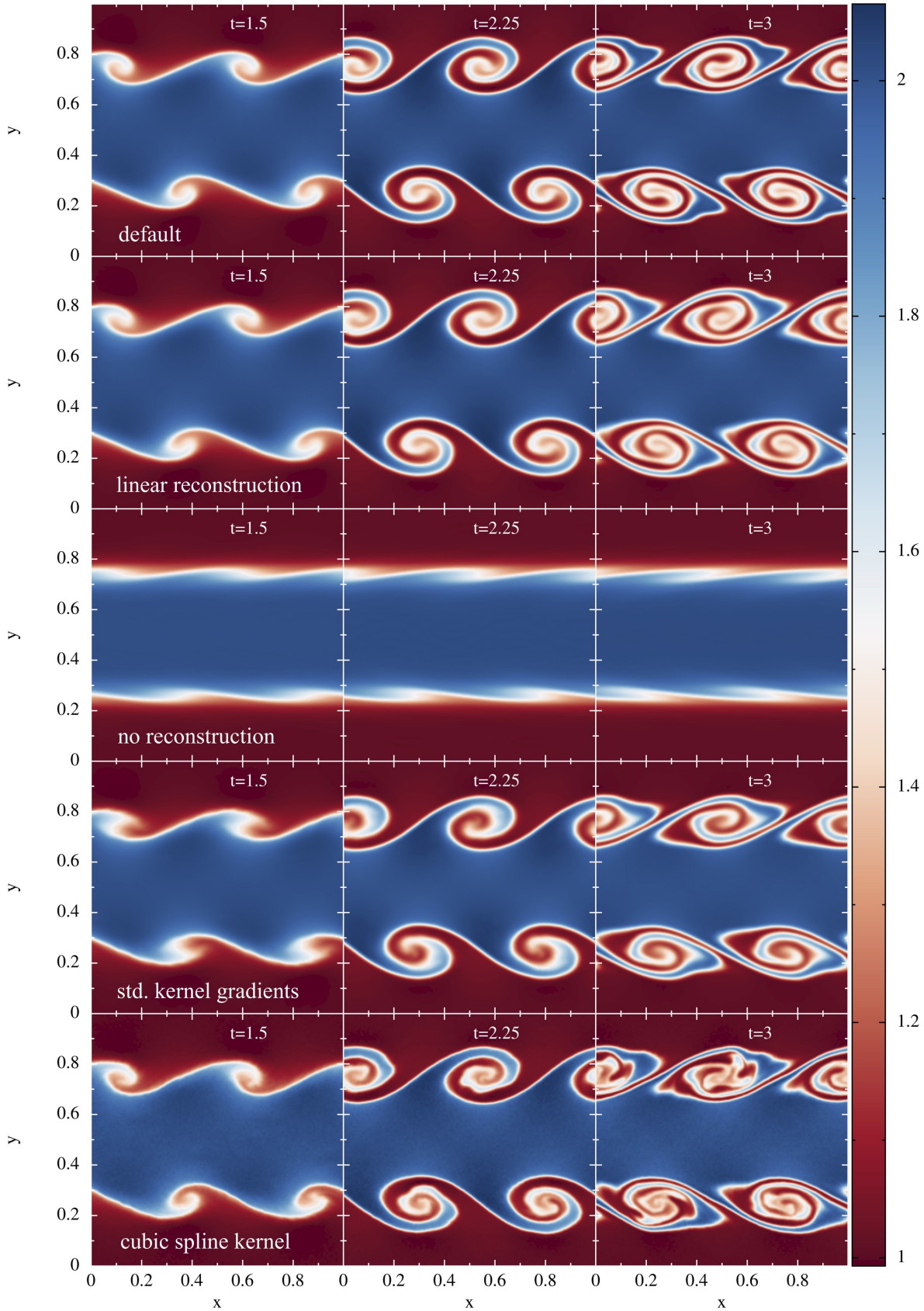


**Figure 14.** 3D Kelvin-Helmholtz test ( $256 \times 256 \times 20$  particles) where we explore the impact of different methodological choices. The first row shows our default choice with matrix-inversion gradients, artificial dissipation that uses a slope-limited, quadratic velocity reconstruction and the 6th order Wendland kernel. Second row: as default, but only using linear reconstruction. Third row: as default, but no reconstruction, just using the velocity differences between particles; this is the conventional way of implementing artificial viscosity in SPH; Fourth row: as default, but using kernel gradients; Fifth row: as default, but using the cubic spline kernel.

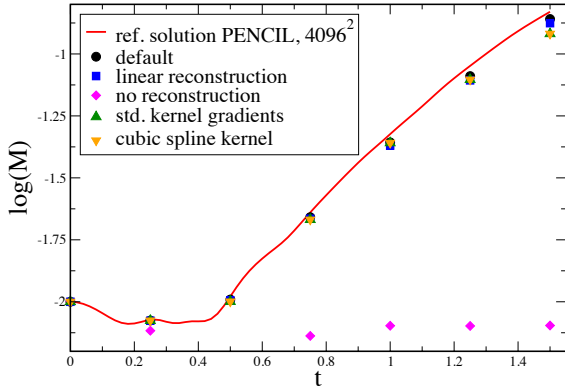


**Figure 15.** Growth of the Kelvin-Helmholtz mode amplitude for the  $256^2$ -case where we vary methodological choices as in Fig. 14. Our default (black circles) is closest to the reference solution, closely followed by the case with only linear reconstruction (blue square). Both the case with standard kernel gradients (green triangles) and the one using the cubic spline kernel (orange triangles) grow somewhat slower. The largest impact in this test, however, has the velocity reconstruction: if it is not applied and the standard SPH prescription is applied instead, the instability is suppressed (magenta diamonds).

We perform this simulation twice, once with the evolution equation set that uses kernel gradients (first row in Fig. 20) and once with the equation set that uses matrix-inversion based gradients (second row). During the first collision the stars become heavily shocked (see panels 1 and 4), vorticity is created and the stellar cores are substantially spun up (panels 2 and 5). During the subsequent evolution the stars fall back towards each other, thereby creating further shocks and vorticity (panels 3 and 6). For this test both equation sets produce very similar results. We have performed these simulations with parameters that we would use for a practical simulation:  $C = 0.2$  in Eq. (28) and a tree opening criterion  $\Theta = 0.9$ , see Gafton & Rosswog (2011) for a detailed description of the used recursive coordinate bisection (RCB) tree. The latter guarantees a fast evaluation of the gravitational forces, though at the price of sacrificing some accuracy. Despite this seemingly tolerant opening criterion, the conservation of both energy and angular momentum for both approaches are better than 0.4%, see Fig. 21, and could be further improved by choosing a stricter force criterion.

### 3.5.3 Tidal disruption of a white dwarf star

As another astrophysical test case we show a tidal disruption of a  $0.5 M_{\odot}$  white dwarf star by a  $1000 M_{\odot}$  black hole. Such encounters can lead to a tidal ignition and explosion of the white dwarf (Luminet & Pichon 1989; Rosswog et al. 2008, 2009) provided that the black hole is of “intermediate” mass (below  $\approx 10^5 M_{\odot}$ ). We show a weak encounter with a “penetration factor”  $\beta = R_t/R_p = 0.9$ , where  $R_t = R_{\text{wd}}(M_{\text{bh}}/M_{\text{wd}})^{1/3}$  is the tidal radius inside of which a star is disrupted by the black hole’s tidal forces. The quantity  $R_p$  is the distance of closest approach (“pericentre distance”). We chose a value of  $\beta < 1$ , since this results in a partial disruption where the star is “nearly disrupted”, but while receding from the black hole its self-gravity overcomes the tidal pull again and a part of the tidal debris re-collapses into a self-gravitating core. Due to the highly

elongated geometry and the small self-gravitating core such partial disruptions pose particular computational challenges.

We model the initial white dwarf as a polytrope with exponent  $\Gamma = 5/3$  with  $5 \times 10^6$  equal-mass SPH-particles. Since for the chosen parameters the pericenter distance is  $R_p > 90GM_{\text{bh}}/c^2$ , we can treat the black hole to excellent accuracy as a Newtonian point mass<sup>6</sup>. Initially the white dwarf is placed at a distance  $r_0 = 6R_t$  which guarantees that the tidal acceleration is only a tiny perturbation ( $\ll 1\%$ ) compared to self-gravity. In Fig. 22, left panel, we show the density in the orbital plane at  $t = 9$  code units (1 code unit = 2.745 s), when the star is approaching the BH, at  $t = 20$ , after the star has just passed it, and at  $t = 47$  when the central region has re-contracted into a self-gravitating core.

### 3.5.4 Double TDE

As a last astrophysical test where the main challenge comes from the widely varying geometry and the involved scales is the disruption of a stellar binary system of two Main Sequence stars by a supermassive black hole. Mandel & Levin (2015) studied tidal interactions of stellar binary systems with massive black holes and found that in a substantial fraction of cases both stars become disrupted. According to their estimate, close to 10% of all stellar tidal disruptions may be double disruption events.

We simulate here the disruption of a binary consisting of two massive stars of  $67.01$  and  $36.8 M_{\odot}$  by a  $M_{\text{bh}} = 10^6 M_{\odot}$  black hole (initial conditions kindly provided by Ilya Mandel). Fig. 23 shows four snapshots of this disruption (color coded is column density). The first shows the stage ( $t = 1.21$  hr) when the stars are approaching the black hole and the leading, more massive star is about to be disrupted. The second snapshot ( $t = 2.77$  hr) shows the leading star being disrupted while the companion is approximately at pericentre. Snapshot three shows both disrupted stars receding from the black hole while in the last snapshot debris is fed in two narrow streams to the hole and an accretion disk is being assembled.

## 4 SUMMARY

In this paper we have presented the new Lagrangian hydrodynamics code *MAGMA2*. It is based on the Smoothed Particle Hydrodynamics method, but benefits from a number of enhancements compared to traditional SPH codes. It uses consistently high-order kernels which substantially reduce noise, though at the price of large neighbour numbers. Our default choice is the Wendland  $C^6$  kernel together with 300 neighbour particles. As a default, we avoid all kernel gradients and instead use much more accurate matrix inversion techniques to calculate gradients. Our equations are formulated in a way that the gradient expressions are anti-symmetric as in standard SPH (i.e. they change sign if the position vectors of two particles,  $\vec{r}_a$  and  $\vec{r}_b$  are interchanged) and this ensures the numerical conservation of physically conserved quantities. Simulations of 3D stellar collisions demonstrate that this new formulation conserves physical quantities equally well as standard SPH formulations.

Our code employs artificial viscosity, but enhanced by techniques that are borrowed from finite volume methods. Instead of employing the velocity difference between two particles in the artificial

<sup>6</sup> For relativistic encounters one can use *MAGMA2* with either the accurate pseudo-potential of Tejada & Rosswog (2013), or, even better, within the approach suggested in Tejada et al. (2017).

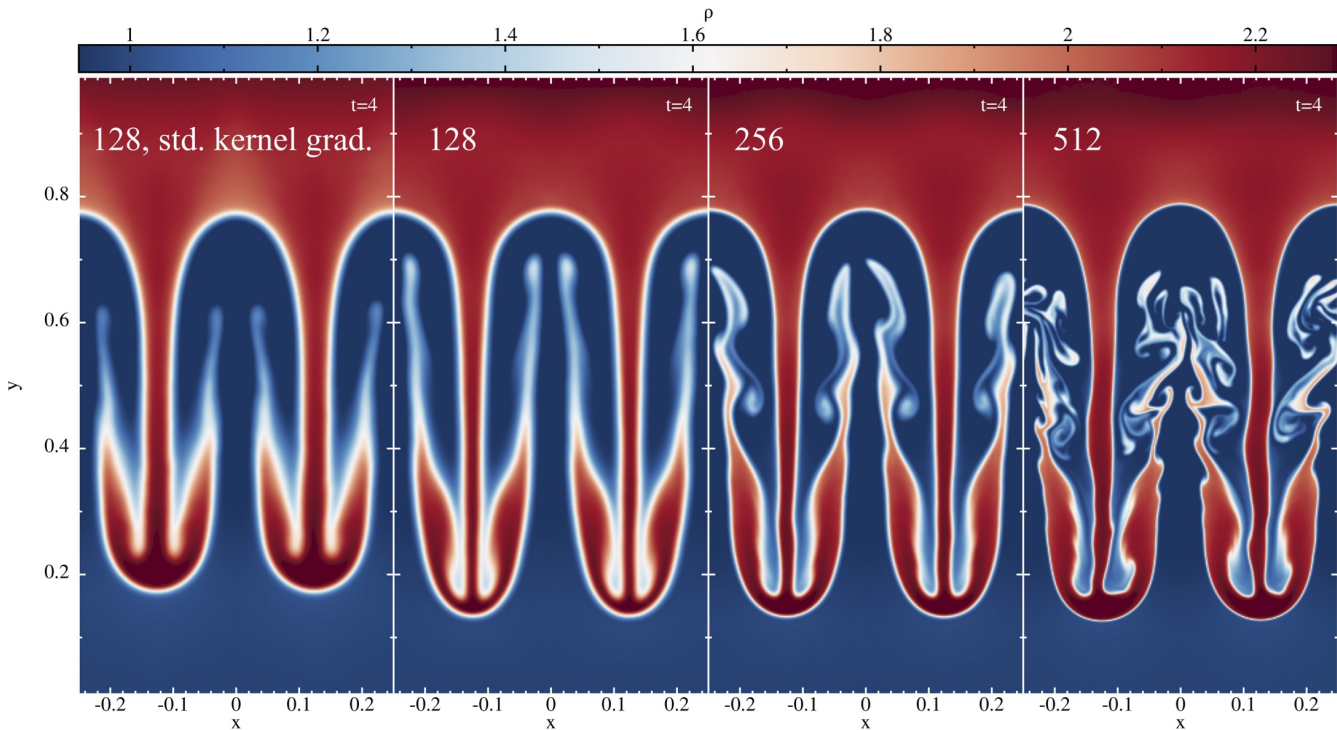


**Figure 16.** The first Rayleigh-Taylor test (first panel) uses kernel-gradients as is common practice in SPH (“ $128 \times 256$ ” particles), all other tests use our default choices of matrix-inversion gradients (“ $128 \times 256$ ”, “ $256 \times 512$ ” and “ $512 \times 1026$ ” particles).

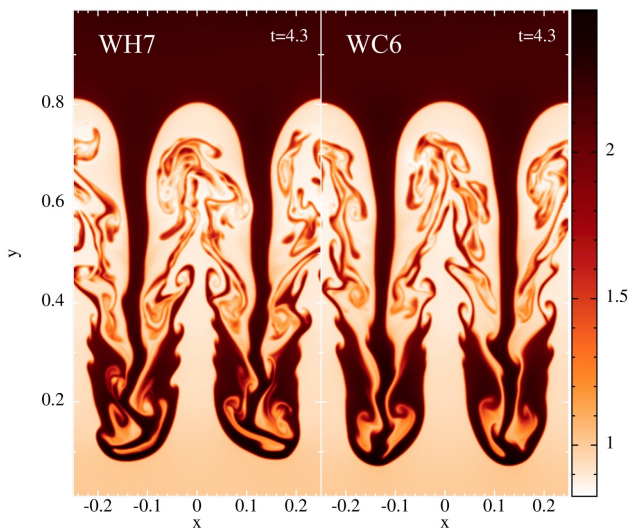


**Figure 17.** Comparison of a Rayleigh-Taylor test (density) at  $t = 4.3$  between a WH7 kernel and our default Wendland  $C^6$  kernel.

viscosity terms, which is the common SPH practice, we use the difference of the *slope-limited, quadratically reconstructed velocities* at the inter-particle midpoint. We find excellent results with this technique, even if large constant values for the dissipation parameters are used. We also apply a small amount of artificial conductivity in MAGMA2. In a separate publication (Rosswog 2019) we explore a novel way to further reduce the effective dissipation. As expected, our code is second order accurate in smooth flows and yields very good results in shocks without any spurious oscillations. It also performs well in Kelvin-Helmholtz and Rayleigh-

Taylor instabilities and in particular yields good results in weakly triggered tests where traditional SPH struggles. While all employed improvements have beneficial effects in these tests, the dominant effect comes from the velocity-reconstruction which substantially reduces the effective dissipation in the flow. We consider our results comparable to those obtained with the CRKSPH-code (Frontiere et al. 2017) that is based on a reproducing kernel methodology.

We have further performed a number of the challenging, vorticity-creating shocks suggested by Schulz-Rinne (1993). Also here, MAGMA2 yields crisp results that are comparable with those from established Eulerian methods. We have also performed a number of more astrophysical simulations (stellar collision and tidal disruptions by black holes) to demonstrate the robustness of MAGMA2 and its accurate numerical conservation.

In none of the comparisons did we find any disadvantage of the matrix-inversion gradient prescription. But in many tests they showed clearly superior performance. Since the matrix inversions are also needed in the dissipation terms even in the conventional kernel-gradient case, we did not find substantial differences in the run time. Where self-gravity is involved it dominates the computational effort so that even a some runtime overhead in the hydrodynamic part would absolutely be worth the effort. As demonstrated in the stellar collision example, both SPH formulations perform equally well in terms of numerical conservation.

In its current version, MAGMA2 has implemented only self-gravitating gas dynamics with polytropic equations of state, but this framework will be enriched in the near future by more physics.

## ACKNOWLEDGEMENTS

It is a great pleasure to thank Ilya Mandel for sharing the initial conditions of the double-TDE and Stephen Justham for providing stel-

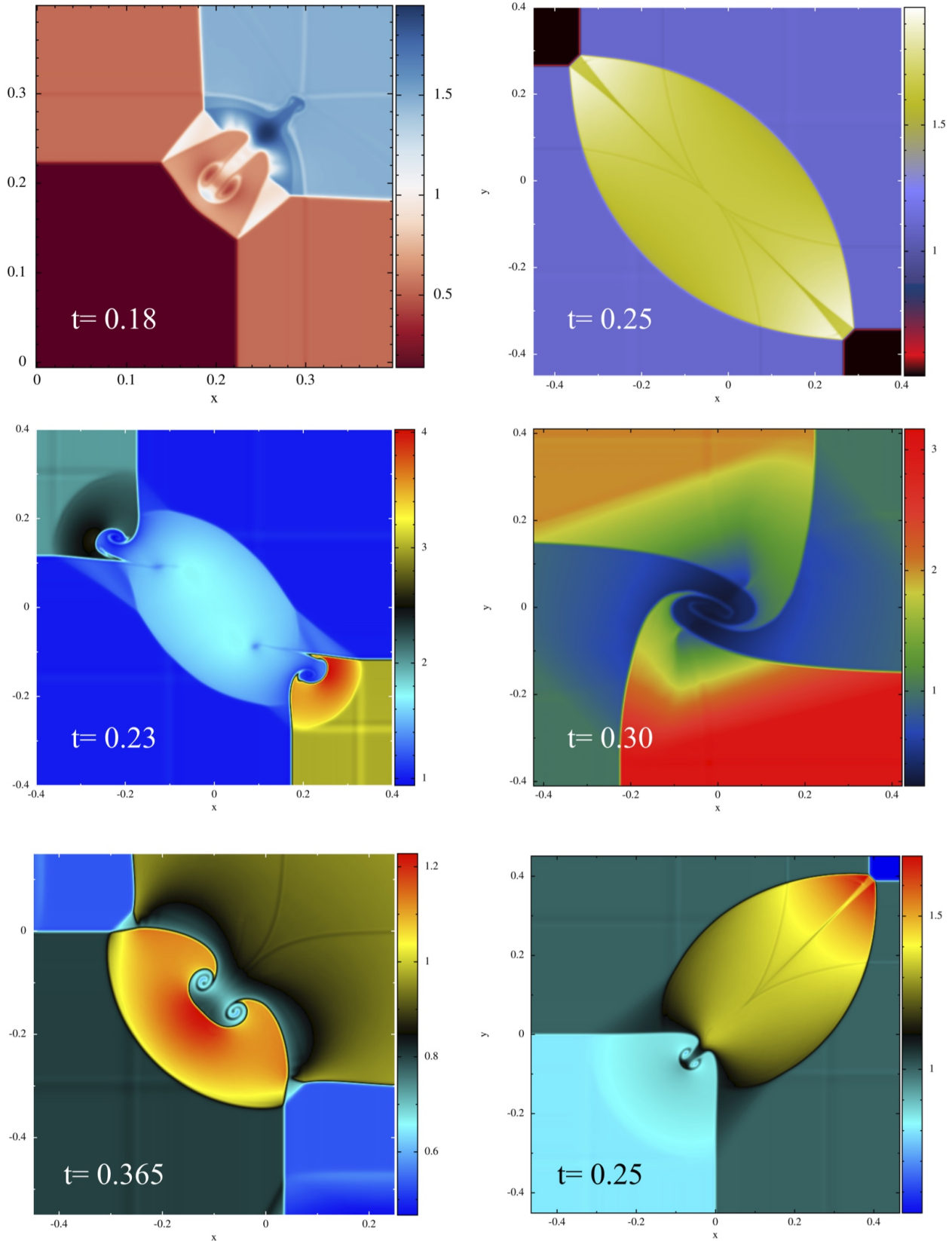


**Figure 18.** MAGMA2 solution (density) for the challenging Schulz-Rinne-type shock tests, see Tab. 1 for the initial conditions. For these tests no exact solutions are known, results need to be compared to other numerical schemes, see e.g. Lax and Liu (1998) or Liska and Wendroff (2003).

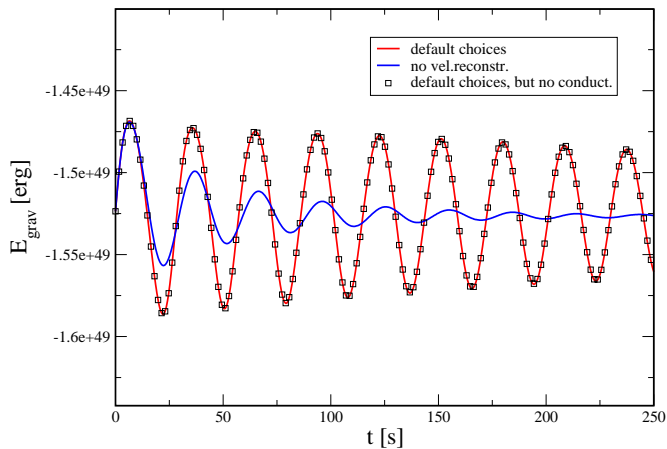


**Figure 19.** Gravitational energy of an oscillating polytropic white dwarf star with 10K particles. The blue line shows artificial viscosity applied as in standard SPH (without velocity reconstruction), the red line is our default choice for methods and parameters and the black squares are our default choices (only every fifth point shown), but without artificial conductivity, i.e.  $\alpha_u = 0$ .

lar profiles of the corresponding masses. Thank you also to Davide Gizzi and Christoffer Lundman for their careful reading of an earlier draft. Some of the figures of this article were produced with the visualization software SPLASH (Price & Monaghan 2007). This work has been supported by the Swedish Research Council (VR) under grant number 2016-03657\_3, by the Swedish National Space Board under grant number Dnr. 107/16 and by the research environment grant "Gravitational Radiation and Electromagnetic Astrophysical Transients (GREAT)" funded by the Swedish Research Council (VR) under Dnr 2016-06012. We gratefully acknowledge support from COST Action CA16104 "Gravitational waves, black holes and fundamental physics" (GWverse) and from COST Action CA16214 "The multi-messenger physics and astrophysics of neutron stars" (PHAROS). The simulations for this paper were performed on the facilities of the North-German Supercomputing Alliance (HLRN), and on the SNIC resources Tetralith and Beskow.

## REFERENCES

- Abel T., 2011, *MNRAS*, 413, 271
- Agertz O., Moore B., Stadel J., Potter D., Miniati F., Read J., Mayer L., Gawryszczak A., Kravtsov A., Nordlund Å., Pearce F., Quilis V., Rudd D., Springel V., Stone J., Tasker E., Teyssier R., Wadsley J., Walder R., 2007, *MNRAS*, 380, 963
- Ben Moussa B., Lanson N., Vila J., 1999, *International Series of Numerical Mathematics*, 29
- Benz W., Bowers R., Cameron A., Press W., 1990, *ApJ*, 348, 647
- Brandenburg A., Dobler W., 2002, *Computer Physics Communications*, 147, 471
- Cabezón R. M., García-Senz D., Escartin J. A., 2012, *A & A*, 545, A112
- Cabezón R. M., García-Senz D., Figueira J., 2017, *A & A*, 606, A78
- Cabezón R. M., García-Senz D., Relano A., 2008, *Journal of Computational Physics*, 227, 8523
- Casanova J., Jose J., García-Berro E., Shore S. N., Calder A. C., 2011, *Nature*, 478, 490
- Cha S.-H., Inutsuka S.-I., Nayakshin S., 2010, *MNRAS*, 403, 1165
- Cha S.-H., Whitworth A. P., 2003, *MNRAS*, 340, 73
- Chow J. E., Monaghan J., 1997, *J. Computat. Phys.*, 134, 296
- Christensen R. B., 1990, *Nuclear Explosives Code Developers Conference*, volume UCRL-JC-105269. Lawrence Livermore National Lab, Lawrence Livermore Technical Report., UCRL-JC-105269
- Cullen L., Dehnen W., 2010, *MNRAS*, 408, 669
- Dehnen W., Aly H., 2012, *MNRAS*, 425, 1068
- Du Q., Faber V., Gunzburger M., 1999, *SIAM Review*, 41, 637
- Frontiere N., Raskin C. D., Owen J. M., 2017, *Journal of Computational Physics*, 332, 160
- Gaburov E., Nitadori K., 2011, *MNRAS*, 414, 129
- Gafton E., Rosswog S., 2011, *MNRAS*, 418, 770
- García-Senz D., Cabezón R., Escartin J., 2012, *A & A*, 538, A9
- Giacomazzo B., Zrake J., Duffell P., MacFadyen A. I., Perna R., 2014, *ArXiv e-prints*
- Gottlieb S., Shu C. W., 1998, *Mathematics of Computation*, 67, 73
- Hernquist L., 1993, *ApJ*, 404, 717
- Hietel D., Steiner K., Struckmeier J., 2000, *Mathematical Models and Methods in Applied Sciences*, 10, 1363
- Hopkins P. F., 2013, *MNRAS*, 428, 2840
- Hopkins P. F., 2015, *MNRAS*, 450, 53
- Hu C.-Y., Naab T., Walch S., Moster B. P., Oser L., 2014, *ArXiv e-prints*
- Hubber D. A., Rosotti G. P., Booth R. A., 2018, *MNRAS*, 473, 1603
- Inutsuka S.-I., 2002, *Journal of Computational Physics*, 179, 238
- Johnson J. R., Wing S., Delamere P. A., 2014, *Space Science Reviews*, 184, 1
- Junk M., 2003, In: Griebel M., Schweitzer M.A. (eds) *Mesh-free Methods for Partial Differential Equations. Lecture Notes in Computational Science and Engineering*, vol 26. Springer, Berlin, Heidelberg, 26, 223
- Kiuchi K., Cerdá-Durán P., Kyutoku K., Sekiguchi Y., Shibata M., 2015, *Phys. Rev. D*, 92, 124034
- Kurganov A., Tadmor E., 2002
- Lax P., Liu X., 1998, *SIAM J. Sci. Comput.*, 19, 319
- Liska R., Wendroff B., 2003, *SIAM J. Sci. Comput.*, 25, 995
- Liu W. K., Jun S., Zhang Y. F., 1995, *International Journal for Numerical Methods in Fluids*, 20, 1081
- Lucy L., 1977, *The Astronomical Journal*, 82, 1013
- Luminet J.-P., Pichon B., 1989, *A&A*, 209, 85
- Mandel I., Levin Y., 2015, *ApJL*, 805, L4
- McNally C. P., Lyra W., Passy J.-C., 2012, *ApJS*, 201, 18
- Monaghan J., 1977, *M.N.R.A.S.*, 181, 375
- Monaghan J., Gingold R., 1983, *J. Comp. Phys.*, 52, 374
- Monaghan J. J., 1992, *Ann. Rev. Astron. Astrophys.*, 30, 543
- Monaghan J. J., 1997, *Journal of Computational Physics*, 136, 298
- Monaghan J. J., 2002, *MNRAS*, 335, 843
- Monaghan J. J., 2005, *Reports on Progress in Physics*, 68, 1703
- Monaghan J. J., Price D. J., 2001, *MNRAS*, 328, 381
- Morris J., Monaghan J., 1997, *J. Comp. Phys.*, 136, 41
- Murante G., Borgani S., Brunino R., Cha S.-H., 2011, *MNRAS*, 417, 136
- Noh W. F., 1987, *Journal of Computational Physics*, 72, 78

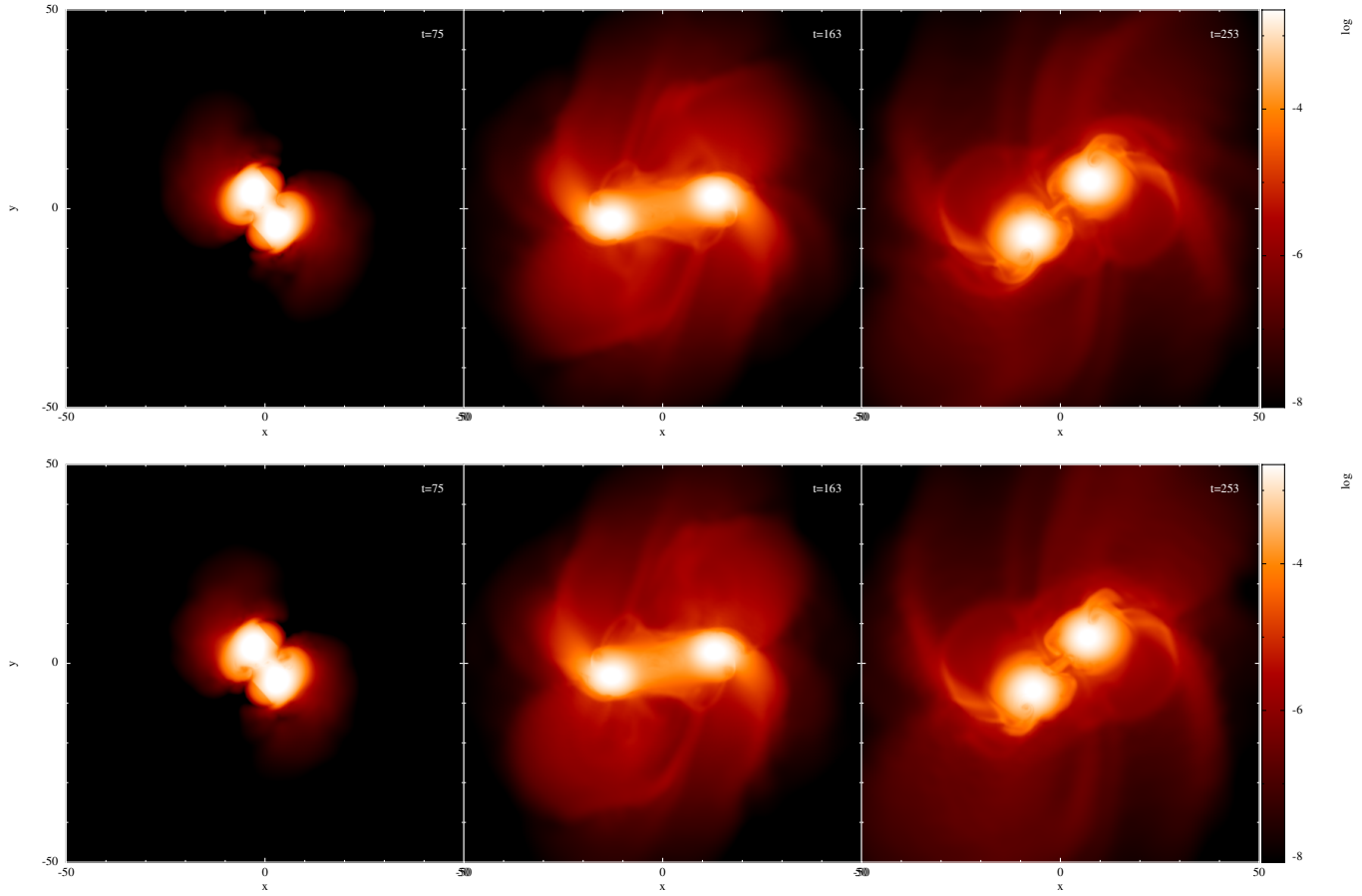


**Figure 20.** Off-center collision between two main sequence stars with an impact strength of  $\beta = 3$ , colour coded is density (in code units:  $1989.1 \text{ g/cm}^3$  for density, time unit is 86.8 seconds). The upper row shows the results from a simulation that uses standard kernel gradients in the evolution equation while the lower row shows the simulation that calculates gradients via a matrix-inversion technique. For this test both methods are in excellent agreement.

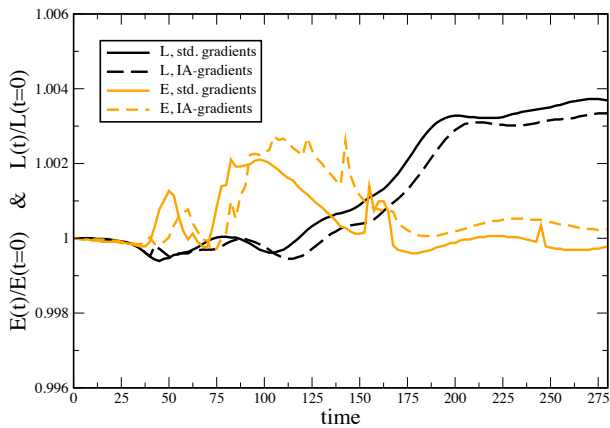


**Figure 21.** Conservation of total energy and angular momentum in the stellar collisions shown in Fig. 20. Both are shown for both simulations (with standard and IA-gradients) and are normalized to their initial values. Time is given in code units of 86.8 seconds.

- Press W. H., Flannery B. P., Teukolsky S. A., Vetterling W. T., 1992, *Numerical Recipes*. Cambridge University Press, New York
- Price D., 2004, PhD thesis, University of Cambridge, arXiv:astro-ph/0507472
- Price D., Monaghan J., 2007, *MNRAS*, 374, 1347
- Price D., Rosswog S., 2006, *Science*, 312, 719
- Price D. J., 2008, *Journal of Computational Physics*, 227, 10040
- Price D. J., 2012, *Journal of Computational Physics*, 231, 759
- Price D. J., Wurster J., Tricco T. S., Nixon C., Toupin S., Pettitt A., 2018, *Publications of the Astronomical Society of Australia*, 35, e031
- Puri K., Ramachandran P., 2014, *Journal of Computational Physics*, 270, 432
- Read J. I., Hayfield T., Agertz O., 2010, *MNRAS*, p. 767
- Ritchie B. W., Thomas P. A., 2001, *MNRAS*, 323, 743
- Rosswog S., 2009, *New Astronomy Reviews*, 53, 78
- Rosswog S., 2015a, *MNRAS*, 448, 3628
- Rosswog S., 2015b, *Living Reviews of Computational Astrophysics* (2015), 1
- Rosswog S., 2019
- Rosswog S., Davies M. B., Thielemann F.-K., Piran T., 2000, *A&A*, 360, 171
- Rosswog S., Price D., 2007, *MNRAS*, 379, 915
- Rosswog S., Ramirez-Ruiz E., Hix R., 2008, *ApJ*, 679, 1385

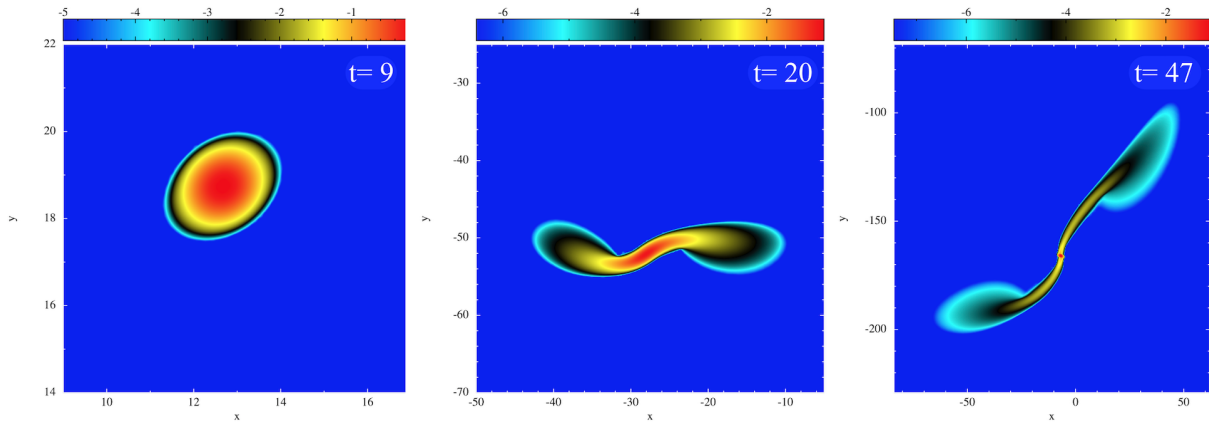


**Figure 22.** 3D tidal disruption of a  $0.5 M_{\odot}$  white dwarf star (modelled with  $5 \times 10^6$  SPH particles) by a  $1000 M_{\odot}$  black hole located at the coordinate origin. This is a weak encounter (penetration factor  $\beta = 0.9$ ) where the white dwarf actually passes outside the tidal radius and becomes "nearly disrupted". After the passage, however, the core contracts again due to self-gravity. Colour-coded is the mass density in the orbital plane.

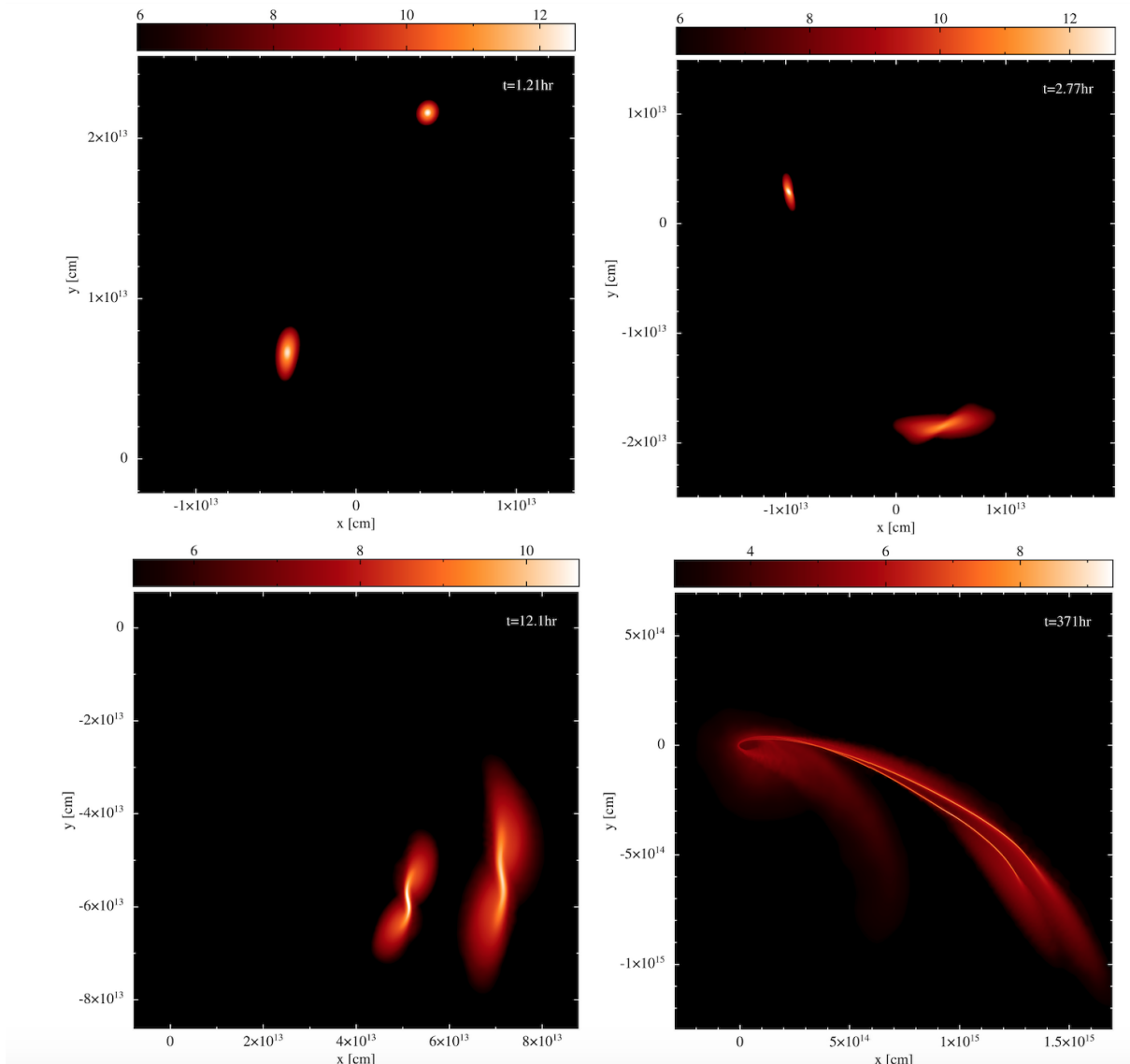


**Figure 23.** Tidal disruption of a binary system consisting of two massive stars ( $67.01$  and  $36.8 M_{\odot}$ ) by a supermassive black hole ( $10^6 M_{\odot}$ ).

- Rosswog S., Ramirez-Ruiz E., Hix R., 2009, *ApJ*, 695, 404  
Saitoh T. R., Makino J., 2013, *ApJ*, 768, 44  
Schoenberg I., 1946, *Quart. Appl. Math.*, 4, 45  
Schulz-Rinne C. W., 1993, *SIAM Journal of Mathematical Analysis*, 24, 76  
Schüssler I., Schmitt D., 1981, *A & A*, 97, 373  
Sedov L. I., 1959, *Similarity and Dimensional Methods in Mechanics*  
Sod G., 1978, *J. Comput. Phys.*, 43, 1  
Springel V., 2010a, *MNRAS*, 401, 791  
Springel V., 2010b, *ARAA*, 48, 391  
Springel V., Hernquist L., 2002, *MNRAS*, 333, 649  
Taylor G., 1950, *Proceedings of the Royal Society of London Series A*, 201, 159  
Tejeda E., Gafton E., Rosswog S., Miller J. C., 2017, *MNRAS*, 469, 4483  
Tejeda E., Rosswog S., 2013, *MNRAS*, 433, 1930  
Toro E., 1999, *Riemann Solvers and Numerical Methods for Fluid Dynamics*. Springer, Berlin  
Tricco T. S., 2019, *MNRAS*, 488, 5210  
Valdarnini R., 2012, *A & A*, 546, A45  
van Leer B., 1974, *Journal of Computational Physics*, 14, 361  
Vila J., 1999, *Mathematical Models and Methods in Applied Science*, 02, 161  
von Neumann J., Richtmyer R. D., 1950, *Journal of Applied Physics*, 21, 232  
Wadsley J. W., Keller B. W., Quinn T. R., 2017, *MNRAS*, 471, 2357  
Wendland H., 1995, *Advances in Computational Mathematics*, 4, 389